Inhibition is the Hallmark of CA3 Intracellular Dynamics Around Awake Ripples

Thesis by
Koichiro Kajikawa

In Partial Fulfillment of the Requirements for the
Degree of
Doctor of Philosophy

CALIFORNIA INSTITUTE OF TECHNOLOGY
Pasadena, California

2022
Defended May 19, 2022

Koichiro Kajikawa
ORCID: 0000-0002-8626-4407

ACKNOWLEDGEMENTS

First, I would like to thank my advisor, Thanos Siapas, for his support and mentorship over all these years. His solid scientific attitude, insatiable passion for experiments and discussions have profoundly influenced my philosophy of science. Furthermore, his generosity and respect for people are incomparable. Without these, I could not balance work and family.

Also, my scientific development and this work owe a tremendous debt to Eugene Lubenov. The meetings with him were simply inspirational. His broad, deep scientific knowledge and clarity of thought brought my science to another level. And his attitude and effort to try to understand my obscure ideas were my salvation.

For their guidance and discussions, I would like to thank Richard Andersen, for mentorship and an outstanding introduction to cortical computation; Michael Dickinson, for insight and encouragement on science and parenting; Betty Hong, for the helping hand to this naive junior scientist; and Markus Meister, whose scientific discussion and advice have influenced me deeply.

I would like to thank my colleagues in the Siapas lab: Brad Hulse, for being my experimental mentor, and for scientific help and advice, continuous kindness, support and friendship (even when I'm not responsive); Jon Kenny, for scientific collaboration, his kindness to me and my family, sharing rumors and introduction to Marvel movies; Britton Sauerbrei, for his introduction to CNS and Siapas Lab, and for being a positive role model for passionate and powerful scientist; Stijn Cassenaer, for scientific advice and Belgian humor; Maria Papadopoulou, for help with immunohistochemistry and lab management; Kevin Shan, for help with all computer-related problems and an engineer's perspective on life; Gustavo Rios, for technical help and frequent chats in front of coffee machine; and Jennifer Mok, for beautiful molecular biological works; advice as a parent senpai. I'd also like to thank my CNS cohort—Joe and Yang— and other Caltech friends—Kyu, Zeynep, Remy, Dong-Wook, Yu, Ryo, Forte, and the Helms family—for being part of my life outside the lab.

Finally, I am deeply grateful to my family — Mikio, Hitomi, Keita and Kanto Kajikawa, Kazuo and Yoriko Iwano — for their constant support and encouragement, and to my wonderful wife Mai and our precious daughter Miki for giving love and joy to my life.

ABSTRACT

Hippocampal ripples are transient population bursts that structure cortico-hippocampal communication and play a central role in memory processing. However, the mechanisms controlling ripple initiation in behaving animals remain poorly understood. Here we combine multisite extracellular and whole cell recordings in awake mice to contrast the brain state and ripple modulation of subthreshold dynamics across hippocampal subfields. We find that entorhinal input to DG exhibits UP and DOWN dynamics with ripples occurring exclusively in UP states. While elevated cortical input in UP states generates depolarization in DG and CA1, it produces persistent hyperpolarization in CA3 neurons. Furthermore, growing inhibition is evident in CA3 throughout the course of the ripple buildup, while DG and CA1 neurons exhibit depolarization transients 100 ms before and during ripples. These observations highlight the importance of CA3 inhibition for ripple generation, while pre-ripple responses indicate a long and orchestrated ripple initiation process in the awake state.

PUBLISHED CONTENT AND CONTRIBUTIONS

Kajikawa, Koichiro and Hulse, Brad K. and Siapas, Athanassios G. and Lubenov, Evgueniy V. Inhibition is the hallmark of CA3 intracellular dynamics around awake ripples. *bioRxiv*, 2021. doi:10.1101/2021.04.20.440699

K.K contributed to the experimental design, data collection, data analysis and writing of the manuscript.

TABLE OF CONTENTS

LIST OF FIGURES

Chapter 1

INTRODUCTION

Memory is one of the key cognitive processes underlying intelligent behavior. Investigation of the hippocampus, the memory center of the brain, provides critical insights into intelligence (Scoville and Milner, 1957; Squire, 1992). Among the hippocampal subfields, CA3 region has attracted attention for its role in memory processes because of the characteristic architecture: CA3 pyramidal cells excite other pyramidal cells and interneurons, and the axons of CA3 pyramidal cells spread throughout most of the region (Lorente de Nó, 1934; Ishizuka, W. M. Cowan, and Amaral, 1995). This recurrent circuit is proposed to work as an attractor network, in which associative memories are stored and recalled ("pattern completion") (Hopfield, 1982; Marr, 1971; Nakazawa et al., 2002; Kesner and Rolls, 2015). Furthermore, recurrent networks have been known for their richer, high-dimensional dynamics than feedforward networks (Dayan and Laurence F Abbott, 2003; Hochreiter and Schmidhuber, 1997). However, they are also difficult to control and design network connectivity that generates desired dynamics and computation (Sompolinsky, Crisanti, and Sommers, 1988; Sussillo and Larry F Abbott, 2009; Werbos, 1990). Therefore, understanding how the biological recurrent networks operate is an intriguing research topic.

In this study, we investigated the membrane potential dynamics of CA3 pyramidal neurons, as well as dentate gyrus (DG) granule cells and CA1 pyramidal cells in awake mice, from two aspects: 1) how do the hippocampal neurons behave corresponding to the input to hippocampus, i.e. entorhinal cortical (EC) input; and 2) how do the hippocampal neurons behave during attractor-like activity pattern known as "ripple".

Neurons communicate with each other via action potentials. An action potential is generated if the total input arriving at the soma exceeds a certain threshold. To understand mechanisms underlying neural network dynamics, the simultaneous measurement of subthreshold activity and neural population activity is critical.

At first, Chapter 2 describes the experimental approach that achieves this aim. Basic properties of recorded neurons are also shown.

Cortico-hippocampal interaction is believed to play a key role in memory consol-

idation (Squire, 1992), however the influence of cortical inputs on hippocampal dynamics in wakefulness is not well understood. Anatomical structure has been classically defined as a trisynaptic excitatory loop that processes higher order sensory information arriving from EC through DG, CA3 and CA1 (Amaral and Witter, 1989), and it is natural to predict that hippocampal neurons follow the EC activity with small delays. At the same time, hippocampus (especially CA3) is expected to exhibit internally-generated autonomous activity beyond input-driven activity (e.g. pattern completion (Kesner and Rolls, 2015), ripples (Buzsáki, 2015), and place cells (Hafting et al., 2005; O'Keefe, 1976)). Addressing how cortical inputs modulate hippocampal dynamics in wakefulness is thus an important step to advancing our understanding of hippocampal information processing.

To this end, Chapter 3 describes the definition of EC input, and characterizes the relationships between EC input and hippocampal activity. These analyses reveal that EC inputs modulate slow membrane potential shifts of hippocampal neurons, and that membrane potential of CA3 pyramidal neurons is modulated by cortical inputs in a way that is largely opposite to the modulation of DG granule cells and CA1 pyramidal neurons.

Ripples are brief (50-100 ms), high-frequency oscillations (80-250 Hz) associated with population bursts in CA1 that play a prominent role in memory consolidation. The prevailing hypothesis is that CA1 ripples are generated by the excitatory input provided by a population burst spontaneously initiated within CA3 excitatory recurrent network. (Buzsáki, 1986; Buzsáki, 2015; Miles and Wong, 1983; Ylinen et al., 1995). However, recent *in vitro* studies have also emphasized the importance of inhibitory neurons in ripple generation process (Bazelot, Teleńczuk, and Miles, 2016; Ellender et al., 2010; Schlingloff et al., 2014), and investigating the subthreshold dynamics of CA3 pyramidal neurons during ripples in awake animals provides insights into biological memory processes.

Therefore, Chapter 4 characterizes the subthreshold activity of hippocampal neurons during ripples. This demonstrates that on average, CA3 pyramidal neuron receives hyperpolarizing input during ripples, and the implications for circuit models of ripple generation are discussed.

Chapter 2

SIMULTANEOUS MULTISITE EXTRACELLULAR AND WHOLE-CELL RECORDINGS ACROSS HIPPOCAMPAL SUBFIELDS

Electrophysiological recordings from behaving animals provide an unparalleled view of neuronal information processing. While recent progress in optical imaging has shown its utility in studying large-scale neural ensemble dynamics (Kim and Schnitzer, 2022; Nieh et al., 2021; Ziv et al., 2013), electrphysiological recording is superior in terms of temporal resolution and is therefore more suitable to study fast, transient events, such as ripples.

Extracellular recording picks up two distinct classes of neuronal signals: spikes, the high frequency (> 0.5 kHz) signal: and the local field potential (LFP), the low frequency (< 200 Hz) signal. The current view is that LFP is generated by synchronized synaptic currents (Buzsáki, Anastassiou, and Koch, 2012; Katzner et al., 2009; Mitzdorf, 1985), and different LFP patterns are observed over different behavioral states (Siapas and M. A. Wilson, 1998; Siapas, Lubenov, and M. A. Wilson, 2005; Vanderwolf, 1969).

Intracellular recording allows direct measurement of the membrane potential and currents of individual neurons. The patch-clamp technique, initially developed to record currents from single membrane channels (Neher and Sakmann, 1976), has been applied to study whole-cell membrane potential and currents (Edwards et al., 1989; Hamill et al., 1981). Furthermore, it has recently become possible to achieve whole-cell patch-clamp recordings in behaving animals, offering new insights into the cellular and circuit mechanisms underlying neural activity in behaving animals (Aksay et al., 2001; Crochet et al., 2011; Harvey et al., 2009; Hulse, Moreaux, et al., 2016; Hulse, Lubenov, and Siapas, 2017).

Given these different measured signal modalities, the combination of intracellular and extracellular recording enables us to study the brain across multiple levels, from single neuron to circuit to behavior.

Here, we combined whole-cell recordings of principal neurons across DG (22 cells), CA3 (32 cells), and CA1 (32 cells) with multisite extracellular LFP recordings spanning the radial extent of dorsal CA1 and DG in awake head-fixed mice that were free to run on a spherical treadmill (Figure 2.1). The location, morphology,

and membrane properties of the recorded cells are described in Figure 2.2 - 2.4).

Experimental Procedures

Head fixation surgery

The methods used were the same as those described in our previous publications (Hulse, Moreaux, et al., 2016; Hulse, Lubenov, and Siapas, 2017). Briefly, male C57Bl/6 mice (Charles River Laboratories) were surgically implanted with a light-weight, stainless steel ring using dental cement. A stainless steel reference wire was implanted over the cerebellum for LFP silicon probe recordings. The locations of future craniotomies for probe and whole-cell recordings were marked. Probe recording coordinates were anterioposterior (AP)/mediolateral (ML): -1.7/1.75 in the left hemisphere for DG; AP/ML: -1.7/2.0 in the left hemisphere for CA1, and AP/ML: -2.15/0.84 in the right hemisphere for CA3. Whole-cell recording coordinates were AP/ML: -1.7/0.65 in the left hemisphere for DG; AP/ML: -1.9/1.5 in the left hemisphere for CA1, and AP/ML: -2.15/3.1 in the right hemisphere for CA3. All coordinates are reported in mm, and all AP and ML coordinates are with respect to bregma. Following surgery, mice were returned to their home cage, maintained on a 12 hour light/dark cycle, and given access to food and water ad libitum. Ibuprofen (0.2 mg/mL) was added to the water as a long-term analgesic. Mice were given at least 48 hours to recover before the day of the experiment.

Exposure surgery

On the day of the recording, while mice (4-8 weeks old) were anesthetized with 1% isoflurane and head-fixed in the stereotaxic apparatus, two small craniotomies (200-500 µm) were made at the previously marked locations and the dura was resected over these locations. For two mice this procedure was carried out three days before the recordings and the mice were habituated to head-fixation on the spherical treadmill for two days to confirm that the short anesthesia on the day of the recordings does not affect the results. A recording chamber was secured on top of the head-fixation device and filled with pre-oxygenated (95% O_2, 5% CO_2), filtered (0.22 µm) artificial cerebrospinal fluid (aCSF) containing (in mM): 125 NaCl, 26.2 $NaHCO_3$, 10 Dextrose, 2.5 KCl, 2.5 $CaCl_2$, 1.3 $MgSO_4$, 1.0 NaH_2PO_4.

Awake, *in vivo* recordings

Awake, *in vivo* electrophysiological recordings were carried out following previously described methods (Hulse, Moreaux, et al., 2016; Hulse, Lubenov, and

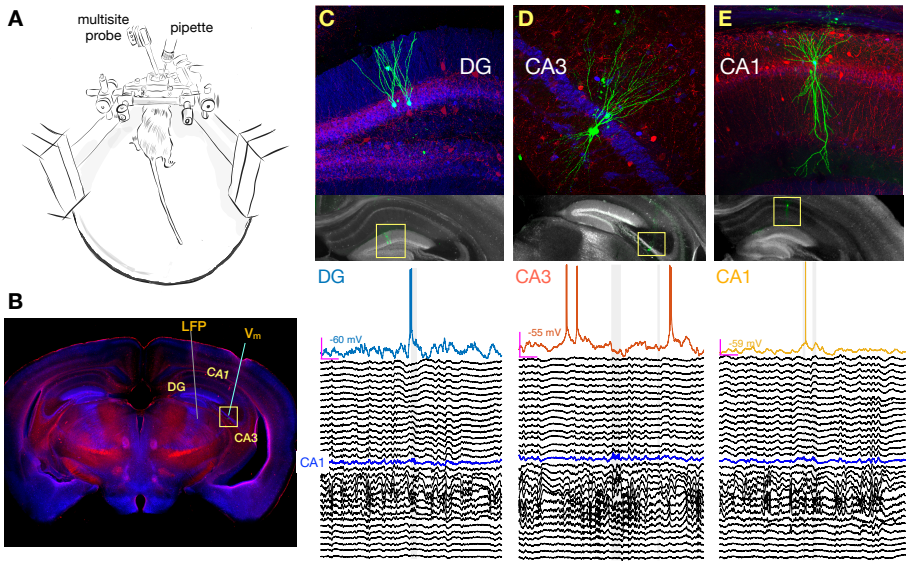

Figure 2.1: **Simultaneous Multisite Extracellular and Whole-Cell Recordings Across Hippocampal Subfields.**
(A) Schematic of setup for simultaneous intracellular and extracellular recordings from awake head-fixed mice free to run on a spherical treadmill.
(B) Typical penetration paths of multisite probe for LFP recordings and micropipette (targeting CA3 in this example for the neuron shown in D) for whole cell recordings. Histological sections were stained for biocytin (green), calbindin (blue), and parvalbumin (red).
(C) Examples of histology and recordings. Top: Recorded DG granule cells are labeled with biocytin and their location and morphology is visualized with fluorescence microscopy. Bottom: Membrane potential (Vm) of a DG granule cell together with simultaneous LFP recordings spanning both CA1 and DG. The blue trace marks the pyramidal cell layer of CA1 where ripples are detected and marked by the gray vertical shading. Notice that the cell fires right before the onset of a ripple. The magenta bars indicate 200 ms and 20 mV, and the baseline Vm is reported next to the trace (-60 mV). The vertical spacing between LFP traces is 100 µm.
(D) Same as C, but for a pyramidal neuron in CA3. Notice that the cell is hyperpolarized following the ripple onset.
(E) Same as C, but for a pyramidal neuron in CA1. Notice that the cell fires inside one of two nearby ripples.

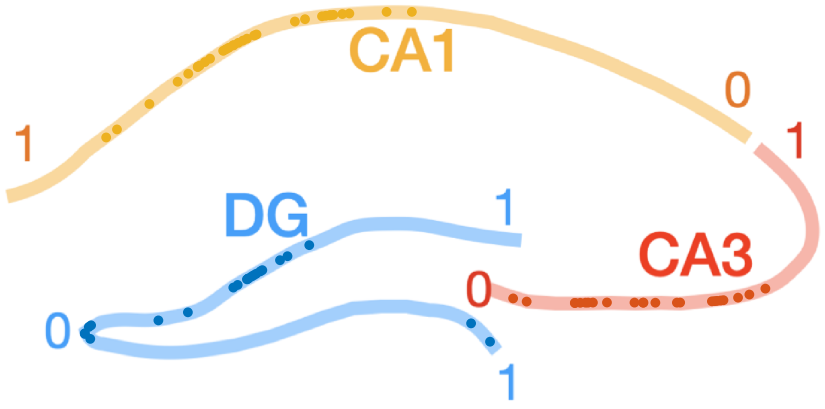

Figure 2.2: **Proximodistal Locations of Recorded Neurons.**
Colored lines illustrate the principal cell layers in DG, CA3, and CA1 through a coronal section. Each cell is assigned a normalized proximodistal location with 0 corresponding to the proximal end and 1 to the distal end of each subfield (as indicated by the numbers) and then plotted as a dot. This is only a schematic since not all cells were recorded from the same dorsoventral level.

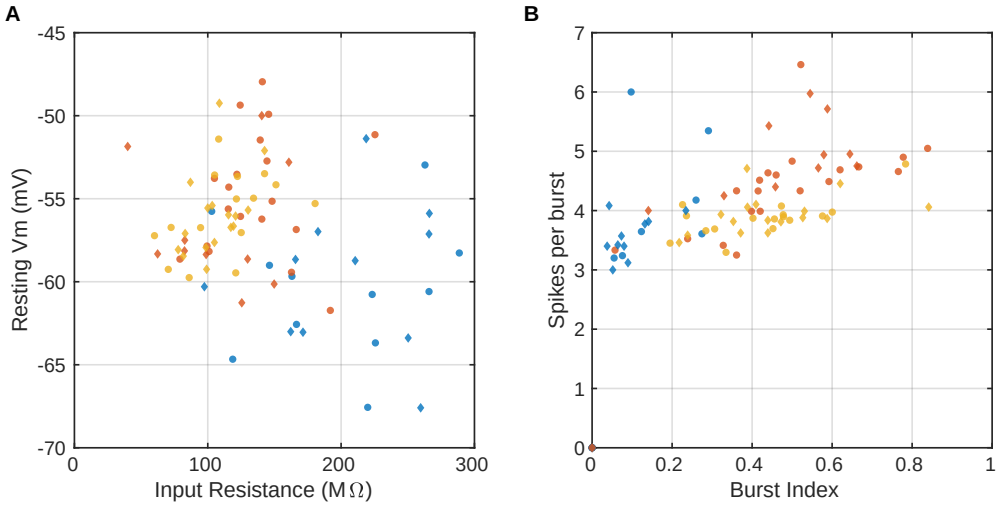

Figure 2.3: **Properties of Recorded Cells.**

Figure 2.3: **(continued)**
(A) Scatter plot shows the input resistance and resting potential for all recorded neurons (markers), color-coded by subfield (DG-blue, CA3-red, CA1-yellow). The example neurons from Figure 2.4 are plotted as diamonds, while the remaining cells are plotted as dots. Notice that the morphologically identified cells (diamonds) have similar properties as the rest of the cells from the respective subfield (dots). There were no significant differences between the two groups ($p > 0.05$ t-test; $p > 0.05$ Wilcoxon rank sum test).
(B) Same as A showing the burst index and average number of spikes per burst for all recorded neurons. The burst index is the fraction of spikes that are part of complex spike bursts. Complex spike bursts are defined as groups of 3 or more spikes with interspike intervals shorter than 20 ms and decreasing spike amplitudes for at least the first 3 spikes in the burst. There were no significant differences between the two groups ($p > 0.05$ t-test; $p > 0.05$ Wilcoxon rank sum test).

Siapas, 2017). Mice were head-fixed on a spherical treadmill secured on an air table (TMC).To measure pupil diameter and whisker movements, the mouse was illuminated with an infrared (850 nm) LED (M85OL3, Thorlabs) and imaged with a CCD camera (scA640-70fm, Basler; with a Nikon AF Micro-Nikkor 105mm f/2.8 lens) positioned 60 degrees from the midline (mouse's left) and 30 degrees down from the horizontal plane (Sakatani and Isa, 2004).

A single-shank, 32-site silicon probe (NeuroNexus) with 100 μm site spacing was inserted in the coronal plane (15 degree angle pointing away from the midline) to a depth of 2600-3400 m and was adjusted for reliably recording LFP ripple oscillations in CA1. To find the rough target depth of whole-cell recording, at first juxtacellular recordings (Pinault, 1996) were performed with pipettes filled with artificial cerebrospinal spinal fluid (aCSF). Whole-cell patch-clamp recordings were performed with a blind-patch approach (Pinault, 1996; Margrie, Brecht, and Sakmann, 2002) in current clamp mode after the target depth had been identified. Pipettes had a resistance of 5-8 MΩ and were filled with an internal solution containing (in mM) 115 K-Gluconate, 10 KCl, 10 NaCl, 10 Hepes, 0.1 EGTA, 10 Tris-phosphocreatine, 5 KOH, 13.4 Biocytin, 5 Mg-ATP, 0.3 Tris-GTP. The internal solution had an osmolarity of 300 mOsm and a pH of 7.27 at room temperature. Pipettes are pulled from borosilicate capillaries (OD: 1.0 mm, ID: 0.58 mm; Sutter Instrument Company) using a Model P-2000 puller (Sutter Instrument Company) and inserted into the brain in the coronal plane with a 15 degree angle pointing towards the midline. Recordings were made using a Multiclamp 700B amplifier (Molecular Devices). The Vm was not corrected for liquid junction potential. Capacitance neutralization

was set prior to establishing the GΩ seal.
The input resistance was estimated by subtracting the access resistance from the ratio of the change in Vm produced by the current step over the magnitude of injected current.

Signal acquisition

All electrophysiological signal acquisition was performed with Labview (National Instruments). Electrophysiological signals were sampled simultaneously at 25 kHz with 24 bit resolution using AC (PXI-4498, internal gain: 30 dB, range: +/- 316 mV) or DC-coupled (PXIe-4492, internal gain: 0 dB, range: +/- 10 V) analog-to-digital data acquisition cards (National instruments) with built-in anti-aliasing filters for extracellular and intracellular/juxtacellular recordings, respectively.

Histology and imaging

To identify the recorded neurons, histology and imaging were performed, as previously described (Horikawa and Armstrong, 1988; Hulse, Moreaux, et al., 2016; Hulse, Lubenov, and Siapas, 2017). Following the experiment, mice were deeply anesthetized with 5% isoflurane, decapitated, and the brain extracted to 4% PFA. Brains were fixed at 4° C in 4% paraformaldehyde overnight and transferred to 0.01 M (300 mOsm) phosphate buffered saline (PBS) the next day. Up to one week later, brains were sectioned coronally (100 m) on a vibrating microtome (Leica), permeabilized with 1% Triton X-100 (v/v) in PBS for 1-2 h, and incubated for more than 3 h at room temperature in PBS containing avidin-fluorescein (1:200, Vector Laboratories), 5% (v/v) normal horse serum (NHS), and 0.1% Triton X-100. Sections were rinsed in PBS between each step. The next day, sections containing biocytin stained neurons were identified on an inverted epifluorescent microscope (Olympius IX51) for further immunohistochemical processing. Sections underwent immunohistochemical staining against calbindin (CB) and parvalbumin (PV) to aid in locating the recorded neurons in the hippocampus. Sections containing biocytin-stained neurons were first incubated in blocking solution containing 5% NHS, 0.25% Triton X-100, and 0.02% (wt/v) sodium azide in PBS. Next, slices were incubated in PBS containing primary antibodies against CB (Rabbit anti-Calbindin D-28k, 1:2000, Swant) and PV (Goat anti-parvalbumin, 1:2000, Swant) overnight. After thorough rinsing in PBS, slices were incubated in PBS containing secondary antibodies CF543 donkey anti-rabbit (1:500, Biotium) and CF633 donkey anti-goat (1:500, Biotium). Processed slices were rinsed and mounted in antifading mounting

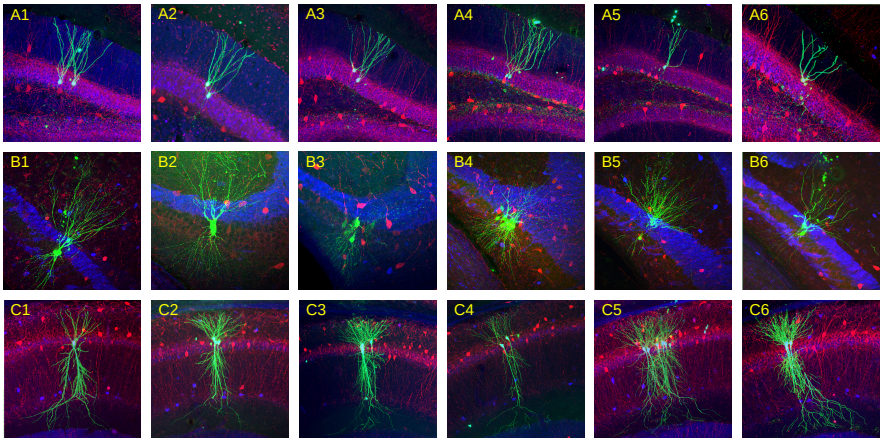

Figure 2.4: **Morphology of Recorded Neurons.**
Histological sections show neurons patched in DG (A1-A6), CA3 (B1-B6), and CA1 (C1-C6). Patched cells were filled with biocytin (green) and sections were also stained for calbindin (blue) and parvalbumin (red). Calbindin labels DG axons, seen as a blue band above the pyramidal cell layer in CA3. Notice that in some experiments multiple neurons are patched and labeled. Their identities can still be confirmed when all labeled neurons belong to the same morphological class as illustrated here.

medium (EverBrite, Biotium). Stained slices were imaged on an inverted confocal laser-scanning microscope (LSM 710 LSM 880, Zeiss).

Chapter 3

ENTORHINAL INPUT DIFFERENTIALLY MODULATES SLOW MEMBRANE POTENTIAL SHIFTS ACROSS HIPPOCAMPAL SUBFIELDS

Bidirectional interactions between the hippocampus and neocortical areas are believed to play a key role in memory consolidation (Squire, 1992). Hippocampal ripples are deemed essential for this process because the associated population activity reflects prior experience (Foster, 2017; Kudrimoti, Barnes, and McNaughton, 1999; Lee and M. A. Wilson, 2002; M. A. Wilson and McNaughton, 1994) and ripple disruption results in memory deficits (Ego-Stengel and M. A. Wilson, 2010; Girardeau et al., 2009; Jadhav et al., 2012). Ripples provide synchronous volleys that drive cortical targets and cooccur with distinct cortical network patterns (Battaglia, Sutherland, and McNaughton, 2004; Jiang, Gonzalez-Martinez, and Halgren, 2019; Ji and M. A. Wilson, 2007; Logothetis et al., 2012; Mölle et al., 2006; Shein-Idelson et al., 2016; Siapas and M. A. Wilson, 1998; Wierzynski et al., 2009). In particular, ripples normally occur during slow-wave sleep (SWS) and quiet wakefulness when hippocampal local field potentials (LFPs) display large-amplitude irregular activity (LIA) (Buzsáki, 1986; Jarosiewicz and Skaggs, 2004; Kay et al., 2016; O'Keefe, 1976; Vanderwolf, 1969), whereas neocortical dynamics are marked by the presence of UP and DOWN states (UDS), alternating periods of elevated and depressed network activity that can also be observed under anesthesia (R. L. Cowan and C. J. Wilson, 1994; Steriade, Nunez, and Amzica, 1993b; Steriade, Nunez, and Amzica, 1993a). Neocortical and hippocampal dynamics can be coordinated via the entorhinal cortex (EC), the main gateway between neocortical areas and the hippocampus, which provides direct input to the dentate gyrus (DG), and areas CA3 and CA1 (Amaral and Witter, 1989). Experiments in sleeping and anesthetized animals show that the EC also exhibits UDS that modulate activity across hippocampal subfields (Hahn, McFarland, et al., 2012; Isomura et al., 2006). However, the influence of cortical UDS on hippocampal dynamics and ripple generation in wakefulness are not well understood.

Below we show that entorhinal inputs to DG exhibit UP and DOWN dynamics during quiet wakefulness, with ripples occurring exclusively in the UP state. Analysis of how these brain states influence membrane potential dynamics reveals that CA3

neurons hyperpolarize in the UP state when ripples occur, in contrast to neurons in DG and CA1.

3.1 Entorhinal Inputs to DG Exhibit UP and DOWN Dynamics During Quiet Wakefulness

Based on LFP dynamics, the network state of the hippocampus can be classified as large irregular activity (LIA), small irregular activity (SIA), or theta rhythmic, with LIA and SIA being the predominant states during quiet wakefulness (Buzsáki, 1986; Jarosiewicz and Skaggs, 2004; Kay et al., 2016; O'Keefe, 1976; Vanderwolf, 1969). Since this classification is typically based on a single hippocampal LFP, it does not consider the origin of the observed field fluctuations, but only their amplitude and frequency content. As a consequence, synaptic currents due to inputs from the entorhinal cortex (EC) as well as other hippocampal subfields are reflected in the local field and cannot be dissociated. In order to address this, we used multisite LFP recordings and computed the laminar current source density (CSD) (Mitzdorf, 1985; Pettersen et al., 2006) throughout CA1 and DG, which in combination with the known circuit anatomy allowed us to infer the spatiotemporal pattern of synaptic activity. An example estimate of this laminar CSD is illustrated in Figure 3.1, which shows several sharp wave-ripples (SWRs) associated with pronounced current sinks in stratum radiatum (sr) of CA1 due to CA3 synaptic input, occurring against a background of synaptic activity in DG. On a longer timescale the CSD clearly reveals alternating periods of high and low rates of transient synaptic activity lasting several seconds (Figure 3.1B) that are particularly prominent within the DG. Strikingly, these alternating periods appear to coincide with slow shifts in the membrane potential of an example CA3 pyramidal neuron (Figure 3.1B). To quantify the level of cortical input to the hippocampus, we averaged the rectified CSD over the molecular layer of DG (Figure 3.1). This measure reflects the magnitude and rate of transient synaptic currents due to inputs from layer II of the lateral and medial EC arriving at the outer two thirds of the dentate molecular layer (Steward, Cotman, and Lynch, 1976; Sullivan et al., 2011; Tamamaki and Nojyo, 1993), as well as associational and return currents flowing in the inner third. Confirming our observations, the rectified DG CSD magnitude showed strong coherence with the subthreshold membrane potential of the example CA3 neuron for frequencies below 1 Hz (Figure 3.11AB). This result was consistent across DG, CA3, and CA1 cells (Figure 3.11B-D).

The distribution of DG CSD magnitude values is fit well by a binary Gaussian

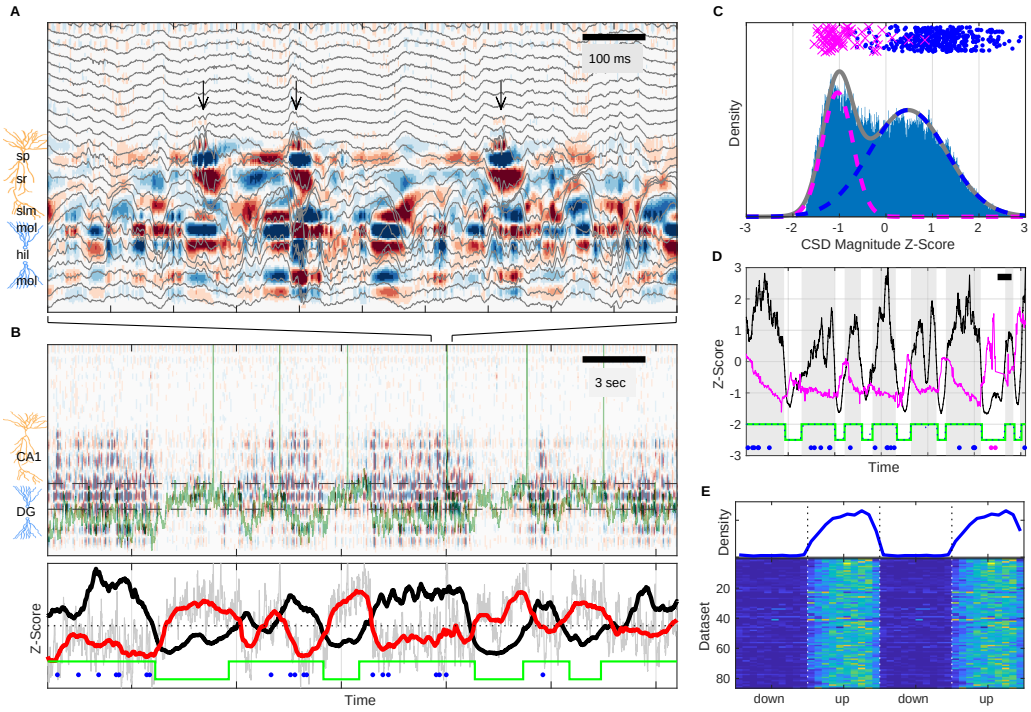

Figure 3.1: **UP and DOWN States Modulate Slow Vm Shifts and Ripple Occurrence.**
(A) Image of current source density (CSD) derived from the LFP traces (gray). Ripples, high-frequency oscillations indicated by the black arrows, are associated with current sinks (red) in stratum radiatum (sr) below the pyramidal cell layer (sp). The bottom third of the image shows large current sources (blue) and sinks (red) within the molecular layers (mol) of DG.
(B) Top: Image of the CSD on a longer timescale reveals alternating periods of high and low CSD activity. The two interrupted black lines mark the vertical extent of the suprapyramidal molecular layer of DG. The Vm of a CA3 neuron is superimposed in green. Notice that periods of low DG CSD activity (light colors) are associated with Vm depolarization. Bottom: DG CSD activity (black), quantified by averaging the rectified CSD over the molecular layer of DG and smoothing, normalized to a z-score. Subthreshold Vm (gray) for the CA3 neuron and its slow component (red) plotted as z-scores. Notice that the black and red traces are anti-correlated. The green stairstep trace marks epochs of elevated DG CSD activity (UP states) and decreased DG CSD activity (DOWN states). Ripples (blue dots) occur in the UP state.
(C) Distribution of DG CSD activity fitted with a two component Gaussian mixture. DG CSD activity at ripples (blue dots) and eye blinks (magenta), show preferential association with the UP and DOWN components, respectively.
(D) Hidden Markov model (HMM) state detection based on DG CSD activity (black). DG CSD activity is high in the UP state (gray stripes), while the pupil (diameter in magenta) dilates at the onset of the DOWN state and then gradually constricts in the course of the UP state. Ripples and eye blinks are marked by blue and magenta dots, respectively. Horizontal scale bar is 3 seconds long.

Figure 3.1: **(continued)**
(E)(Top) Population average probability density of ripple occurrence as a function of UDS phase. Notice that ripples occur almost exclusively in the UP state. (Bottom) Rows in the pseudocolor image show the density of ripple occurrence for each dataset (n=86). Densities are replotted over two UDS cycles.

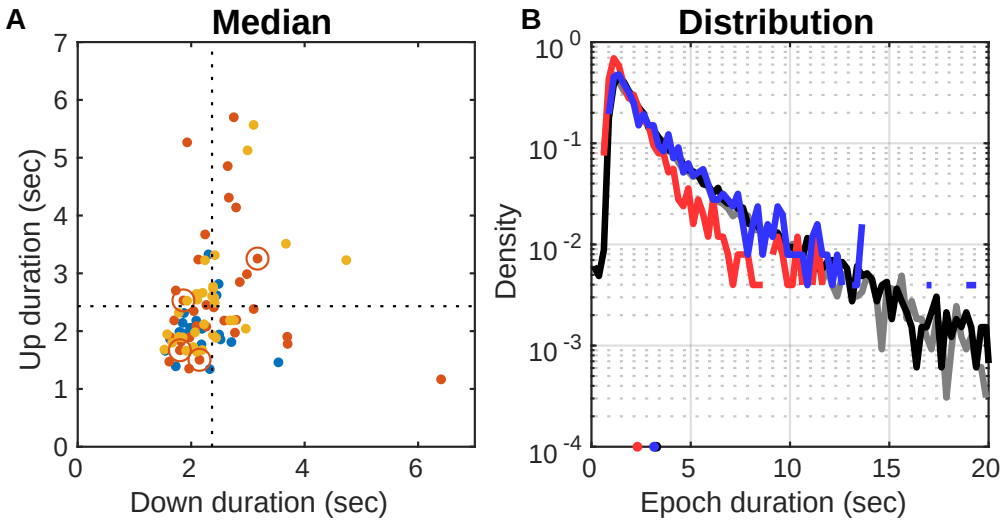

Figure 3.2: **UP and DOWN Epoch Durations.**
(A) Median DOWN epoch duration plotted against median UP epoch duration for each dataset color-coded by subfield of whole-cell target. Population averages are marked by the interrupted lines (UP=2.43 sec, DOWN= 2.37 sec). Open circles mark the datasets for which dura resection occurred 3 days before the experiment (no same day anesthesia, UP = 2.24 sec, DOWN = 2.25 sec). The medians of these 4 marked datasets were not significantly different from the rest (Wilcoxon rank sum test, $p > 0.05$)
(B) Distributions of DOWN (black) and UP (gray) epoch durations pooled across all datasets. Epochs are detected with 250 ms resolution, so the curves at durations shorter than that are affected. Distributions are nearly exponential with similar means (UP = 3.06 sec, DOWN = 3.25 sec) and standard deviations (UP = 3.57 sec, DOWN= 3.48 sec). Outliers (15/13053 UP and 2/13139 DOWN epochs with durations longer than 60 seconds) were excluded. The blue and red lines show the distributions for datasets with no same day anesthesia (means: UP = 2.11 sec, DOWN = 3.15; standard deviations: UP = 1.95 sec, DOWN = 3.11 sec).

mixture (Figure 3.1C) consistent with synaptic activity switching between high and low level regimes. Since EC inputs are responsible for much of the dentate synaptic currents, we identify these regimes as corresponding to entorhinal UP and DOWN states (UDS). Since UDS in EC are coordinated with UDS in other cortical and thalamic areas, we reasoned that the DG CSD contains information about widespread brain state modulation and would therefore be correlated to other brain state signatures and behavioral metrics. Indeed we found that ripples tended to occur almost exclusively when the DG CSD was high (UP state), while eyeblinks had the opposite relationship and occurred when the DG CSD was low (DOWN state) (Figure 3.1C-E, Figure 3.11. Furthermore, the DG CSD showed a strong coherence with the slow changes (below 1 Hz) in pupil diameter (Figure 3.1D, Figure 3.11B).

In order to investigate these effects further we developed an unsupervised method for extracting UP and DOWN states from the DG CSD based on a hidden Markov model (HMM) (Figure 3.1C-D). In addition to identifying state transition points, the segmentation allows the translation of the time axis into a circular UDS phase, so that event distributions can be computed with respect to the UP-DOWN phase. This analysis demonstrates that essentially all ripples occur within the UP state and the rate of ripple occurrence ramps up to a steady state value in the course of the UP state itself and abruptly terminates upon transition to a DOWN state (Figure 3.1E). It also shows that upon transition to the DOWN state the pupil quickly dilates, signaling increased arousal, and then gradually constricts through the course of the UP state, indicating a progressive reduction of arousal and attention to external stimuli through the course of the UP state (Figure 3.15D). Both UP and DOWN epoch durations were distributed approximately exponentially with means of 3.06 sec (UP) and 3.25 sec (DOWN) and these values were consistent across recording sessions (Figure 3.2). These observations show that quiet wakefulness can be reliably decomposed into UP and DOWN states that reflect increased and decreased EC inputs, respectively. This UDS classification reflects the dynamics of the cortical input to the hippocampus, in contrast to LIA/SIA segmentation that is influenced by the states of the hippocampal subfields themselves, which as we describe below are not necessarily coherent. Nevertheless LIA$\rightarrow$SIA transitions mapped closely to UP$\rightarrow$DOWN transitions, with SIA$\rightarrow$LIA transitions also concentrated around DOWN$\rightarrow$UP transitions (Figure 3.3). These observations are consistent with UP states broadly overlapping with LIA and DOWN states with SIA.

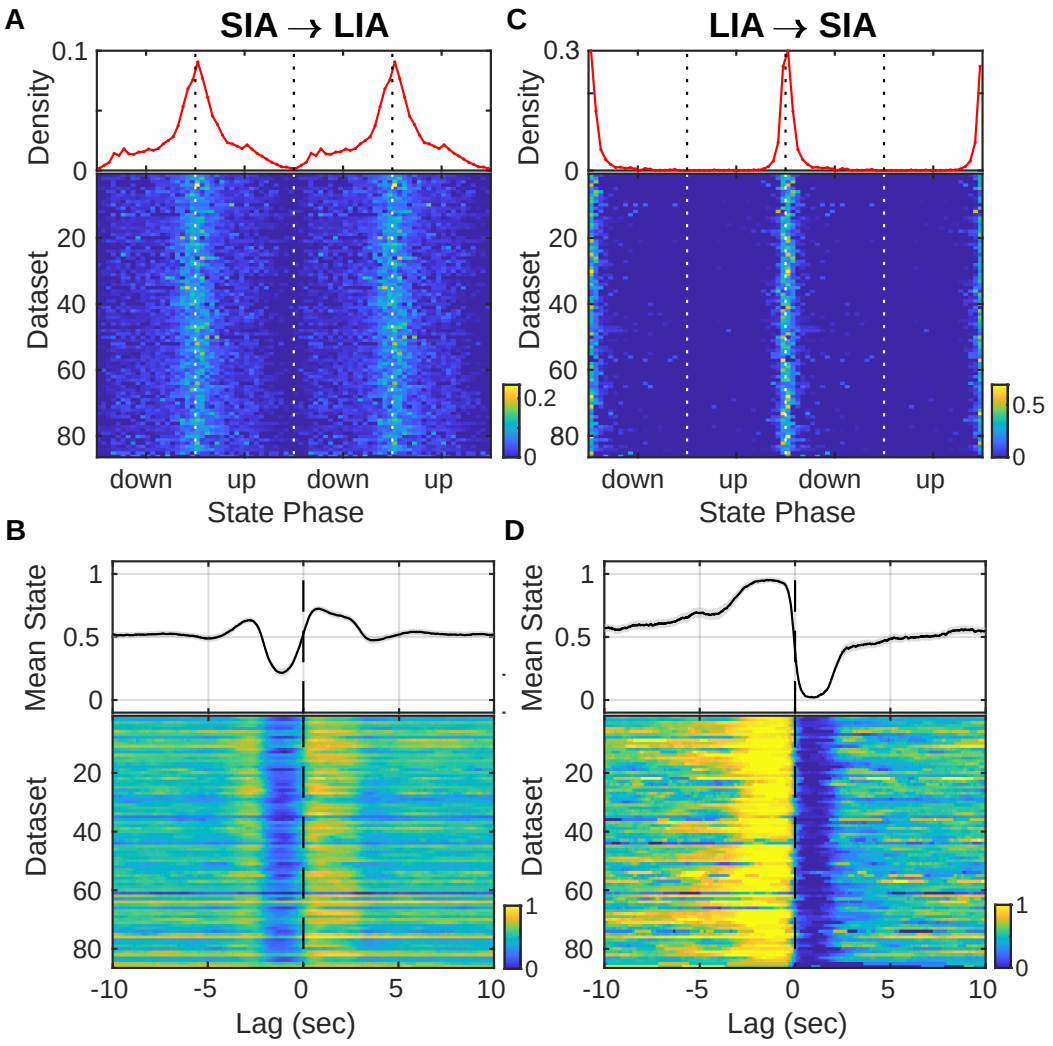

Figure 3.3: **Comparison of LIA/SIA and UP/DOWN transitions.** LIA and SIA states and transitions were extracted based on CA1 LFPs as previously described (Hulse, Lubenov, and Siapas, 2017).
(A) (Top) Average probability of SIA→LIA transition over the UDS cycle. (Bottom) Each row shows the probability of SIA→LIA transition for a given dataset. Notice that SIA→LIA transitions are more likely near DOWN→UP transitions.
(B) Probability of LIA→SIA transition over the UDS cycle. Notice that LIA→SIA transitions are very tightly concentrated near the UP→DOWN transition.

3.2 CA3 Membrane Potential Shifts are Negatively Correlated with Entorhinal Inputs to DG

What is the impact of entorhinal inputs on the activity of hippocampal neurons? The subthreshold membrane potential of the example CA3 neuron in Figure 3.1B is clearly related to the DG CSD and consequently to UP-DOWN states. Importantly, the relation is evident in the slow shifts in Vm and not in the superimposed faster

Figure 3.3: **(continued)**
(C) Expected state centered on SIA→LIA transitions. DOWN states are represented by 0 and UP states by 1, so the expected state is equivalent to the UP state probability. Notice that the UP state probability is depressed before and elevated after the SIA→LIA transition.
(D) Expected state centered on LIA→SIA transitions. Notice that the UP state probability is over 90% before the LIA→SIA transition and drops to 0 right after. These observations are consistent with UP states broadly overlapping with LIA and DOWN states with SIA.

fluctuations. This is confirmed by the fact that all significant coherence between Vm and DG CSD occurs below 1 Hz (Figure 3.11). We therefore separated the fast from the slow dynamics of the subthreshold membrane potential (Vm) fluctuations with a cutoff frequency of approximately 1 Hz (Figure 3.9).

Surprisingly, the Vm of the CA3 pyramidal neuron in Figure 3.1B is more hyperpolarized when DG CSD and hence the excitatory EC input rate is high and, conversely, more depolarized when EC input rate is low. Does EC input impact subthreshold activity in other hippocampal subfields in a similar way? To address this, we computed the cross-covariance between DG CSD activity and the slow Vm component of cells in DG, CA3, and CA1 (Figure 3.4). The majority of DG and CA1 cells (21/22) displayed a strong positive correlation to EC inputs, the majority of CA3 neurons (26/32) exhibited a negative correlation, while CA1 neurons were split in half. In other words, while the slow Vm fluctuations in DG and CA1 are nearly in sync with the DG CSD (Figure 3.4A, 3.4C), they are anticorrelated in CA3 (Figure 3.4B). Furthermore, a closer look at the lag associated with peak absolute correlation reveals that while DG neurons follow the DG CSD very closely (37 ms median lag), the significantly correlated CA1 neurons actually lead the DG CSD (-225 ms median lag), while the trough of the CA3 negative correlation follows the DG CSD (296 ms median lag) (Figure 3.12). This subfield ordering is inconsistent with a simple feedforward activation along the trisynaptic circuit in the awake state.

How well can we estimate the slow Vm component of hippocampal neurons from the DG CSD? All hippocampal subfields receive direct input from the entorhinal cortex (EC), and yet the pattern of modulation by the UP-DOWN state cycle varies across subfields. In order to understand how EC inputs influence hippocampal neurons we used the measured DG CSD as a proxy of EC input and estimated linear transfer models for each cell treating DG CSD activity as input and the cell's slow

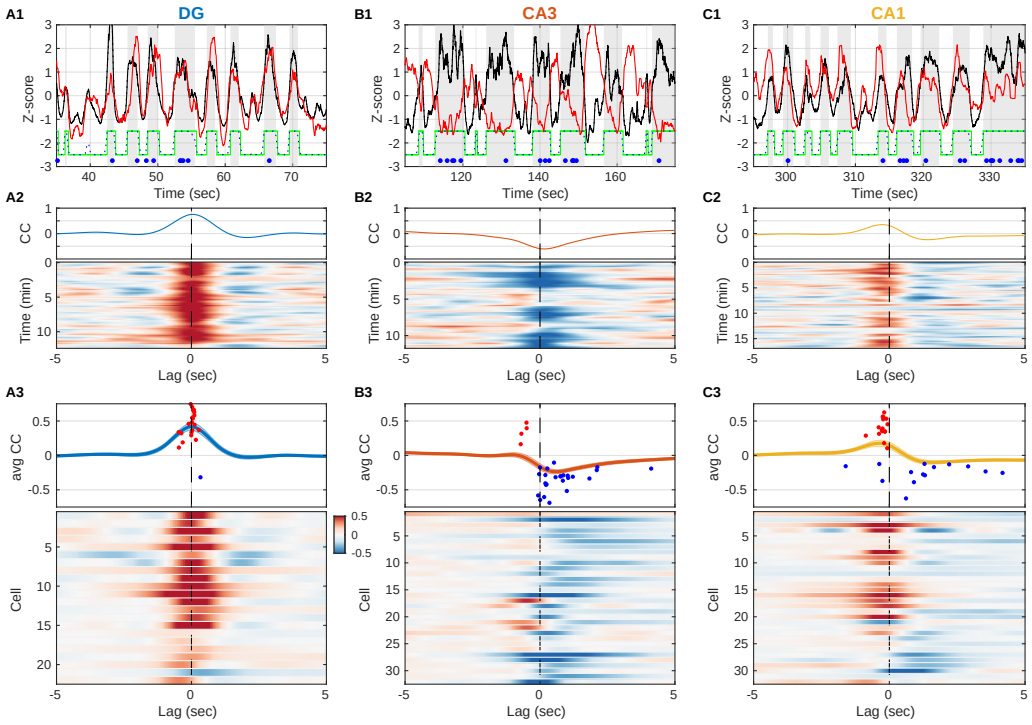

Figure 3.4: **Entorhinal Input to DG is Negatively Correlated with Slow Vm Shifts in CA3 in Contrast to DG and CA1.**
(A1) DG CSD activity (black) and slow component (< 1 Hz) of subthreshold Vm (red) for an example DG granule cell. Gray vertical stripes and green stairstep trace mark periods classified as UP states. Ripples are marked by the blue dots. Notice that the Vm slow component is modulated in lockstep with the DG CSD.
(A2) (Top) Cross-covariance between the slow Vm component of the example cell above and DG CSD activity. (Bottom) Cross-covariances are computed over 30 sec sliding windows and displayed as a pseudocolor image.
(A3) (Top) Population average cross-covariance of all recorded DG granule cells. Bands around the mean curves show the standard error of the mean (SEM). Dots mark the peak (red) or trough (blue) lag and amplitude of individual cells' cross-covariance extrema. (Bottom) Cross-covariances for all DG granule cells stacked vertically and displayed as a pseudocolor image. Notice that most traces are peaked near zero lag. In all figures cells are ordered by their ripple-triggered average response (RTA) rank (Figure 4.1), unless stated otherwise.
(B) Same as A, but for CA3 pyramidal neurons. Notice that the example cell in (B1, B2) and the population overall (B3) have membrane potentials that are anti-correlated with DG CSD activity.
(C) Same as A and B, but for CA1 pyramidal neurons. The Vm of many CA1 neurons is positively correlated with DG CSD activity, but the Vm (red) leads the DG CSD (black) as in C1, so correlation peaks occur at negative lags (C3). A subset of CA1 neurons exhibits negative correlations at positive lags.

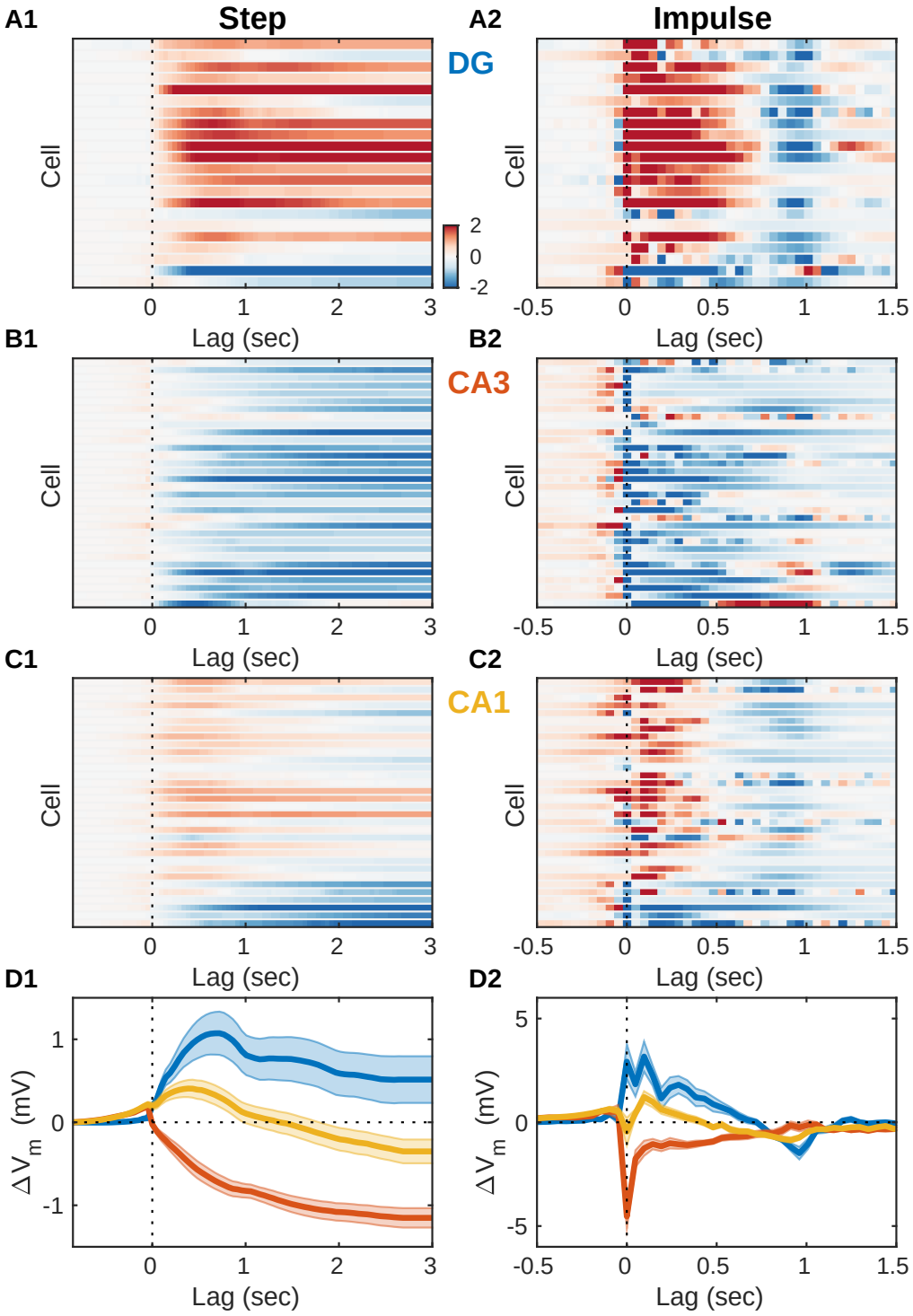

Figure 3.5: **Entorhinal Input Differentially Modulates Slow Vm Shifts Across Hippocampal Subfields.**

Figure 3.5: **(continued)**
(A1) Each row of the pseudocolor image shows the step response of a linear transfer model describing the effect of DG CSD activity on the slow Vm component for a given DG cell. The vertical interrupted line marks the onset of the input step.
(A2) Each row shows the impulse responses of the corresponding models in A1. The vertical interrupted line marks the onset of the impulse. Notice that the majority of DG cells exhibit causal behavior, i.e. the impulse response is near zero for negative lags.
(B) Same as A, but for CA3 pyramidal neurons. Notice that the majority of CA3 neurons hyperpolarize in response to EC input and some cells exhibit non-causal impulse responses, i.e. some impulse responses have non-zero (positive) values at negative lags.
(C) Same as A and B, but for CA1 pyramidal neurons. Notice that some CA1 cells also exhibit non-causal impulse responses.
(D) Area-specific population average step response (D1) and impulse response (D2) color-coded by brain area. Bands around the mean curves show the SEM. Notice the distinct responses across hippocampal subfields.

Vm component as the model output (Figure 3.5). We considered a class of finite impulse response (FIR) models allowing for non-zero filter values at negative lags and hence for a non-causal influence of the input on the output. The estimated impulse responses (Figure 3.5A2-D2) revealed that while DG granule cells had causal responses, many CA3 and CA1 cells showed positive filter values at negative lags (up to -250 ms) signaling a non-causal relation between DG CSD and Vm. This was consistent with the positive/negative peak correlation lags observed for DG/CA1 cells (Figure 3.12A-B), but revealed a non-causal effect in CA3 which was not evident in the cross-covariance analysis. At positive lags the impulse responses for the majority of DG and CA1 cells were positive, while they were negative (inhibitory) for the majority of CA3 pyramidal neurons. The estimated models allowed us to simulate the step responses of hippocampal neurons (Figure 3.5A1-D1) and showed that as a population DG and CA3 exhibited persistent depolarization and hyperpolarization in response to sustained EC input, respectively, while CA1 showed a transient depolarizing response that decayed within 1 second. We also simulated the slow Vm components of hippocampal neurons from DG CSD and found good qualitative agreement with the experimental observations (Figure 3.6), confirming that the transfer models provide a succinct description of the behavior of hippocampal neurons in response to changing EC input levels.

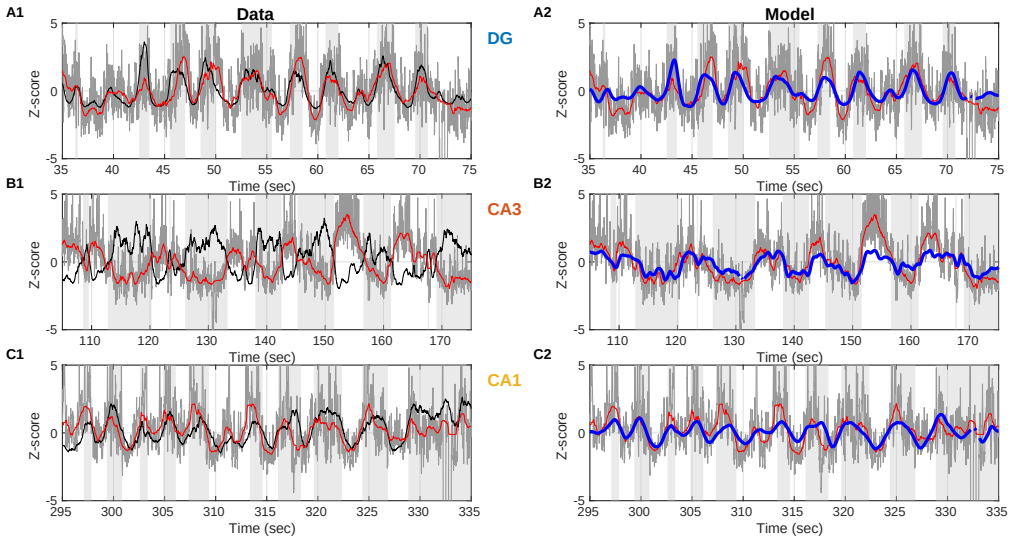

Figure 3.6: **Linear Prediction of Slow Vm Component from DG CSD Activity.** (A1) Data from an example DG granule cell. Vm (with spikes removed) is shown in gray and its slow component in red. DG CSD activity is plotted in black and the UP states are marked by the light gray stripes in the background. All traces are converted to z-scores in order to be compared.
(A2) Same as A1, but the DG CSD trace is omitted and replaced by a linear model prediction of Vm slow (blue) from DG CSD activity.
(B) Same as A, but for an example CA3 pyramidal cell.
(C) Same as A and B, but for an example CA1 pyramidal cell.

3.3 CA3 Pyramidal Neurons Hyperpolarize During UP States

The slow Vm component and firing rate of hippocampal neurons were modulated at UP and DOWN transitions (Figure 3.13) in a way that was consistent with the transfer model predictions (Figure 3.14). To understand their behavior through the course of the UDS cycle, we analyzed the subthreshold membrane potential and spiking of hippocampal neurons as a function of the UDS phase (Figure 3.7). In particular, we computed the distribution of Vm values conditioned on the phase of the UDS cycle. These distributions displayed phase-dependent Vm means for the majority (82/86) of hippocampal neurons (Figure 3.7A1-D1) and many cells (42/86) also exhibited phase-dependent fast Vm component variance (Figure 3.7A2-D2). Several important differences between the hippocampal subfields were evident. Dentate granule cells were quite homogeneous in their behavior through the course of the UP-DOWN state and all but one cell showed sustained Vm depolarization which was maintained through the course of the UP state and was mirrored by a persistent hyperpolarization throughout the DOWN phase (Figure 3.7A1). In contrast, about a third (9/32) of CA3 neurons exhibited the exact opposite behavior:

sustained Vm hyperpolarization through the UP state and depolarization through the DOWN state (Figure 3.7B1). The remaining population exhibited a more transient depolarization with a peak slightly preceding or coincident with the UP transition point (Figure 3.7B1). The CA1 pyramidal cell population displayed a level of diversity that was intermediate to that of DG and CA3. About 40% of CA1 neurons (13/32) were depolarized in the UP state and hyperpolarized in the DOWN state, but the responses were more transient than in DG, with depolarization/hyperpolarization decaying through the course of the UP/DOWN state, respectively (Figure 3.7C1). The behavior of the remaining CA1 neurons appeared similar to that of the CA3 population. With respect to Vm fluctuations, DG granule cells exhibited the highest variability, exceeding that in CA3 and CA1 (Figure 3.8A1-D1). With respect to overall Vm fluctuations only CA1 neurons displayed state-dependent modulation of Vm variability (Figure 3.8D1), with the UP state being associated with more variable Vm. Focusing on the fast Vm component alone, both CA1 neurons (14/32) and DG granule cells (9/22) showed a significant jump in variability during the UP state with no granule cells and only 3 CA1 neurons having the opposite trend (Figure 3.7A2-D2). In contrast, CA3 pyramidal neurons exhibited both jumps and drops and at the population level had a nearly constant level of Vm variability throughout the UP-DOWN state cycle, which equaled that of CA1 in the UP state, but exceeded it in the DOWN phase (Figure 3.7B2, 3.7D2, Figure 3.8D1). Interestingly, with respect to spiking two thirds of the population of DG (15/22) and CA1 (22/32) neurons exhibited similar behavior, a significant increase in firing rate that persisted through the course of the UP phase (Figure 3.7A3-D3). In contrast, the firing behavior of CA3 neurons largely mirrored the behavior of the Vm mean, with about a half of CA3 neurons (17/32) exhibiting a significant increase in firing rate in the DOWN state and the remaining population showing a transient increase peaking near the UP transition point (Figure 3.7B3, 3.7D3). Thus CA3 neurons were maximally hyperpolarized and had lowest firing probability at the end of the UP phase when the rate of ripple occurrence was highest (Figure 3.1E).

Figure 3.7: **Hippocampal Subfields Exhibit Distinct Activity Profiles over the UDS Cycle.** (A1) Vm mean as a function of UDS phase for each DG granule cell displayed as a row in the pseudocolor image. Cells are ordered by the first principal component coefficient of the image matrix (UDS rank). (A2) Fast Vm component standard deviation as a function of UDS phase for DG granule cells. (A3) Observed spiking probability for all DG granule cells displayed as a pseudocolor image. Grayed out rows correspond to cells that fired fewer than 100 spikes.

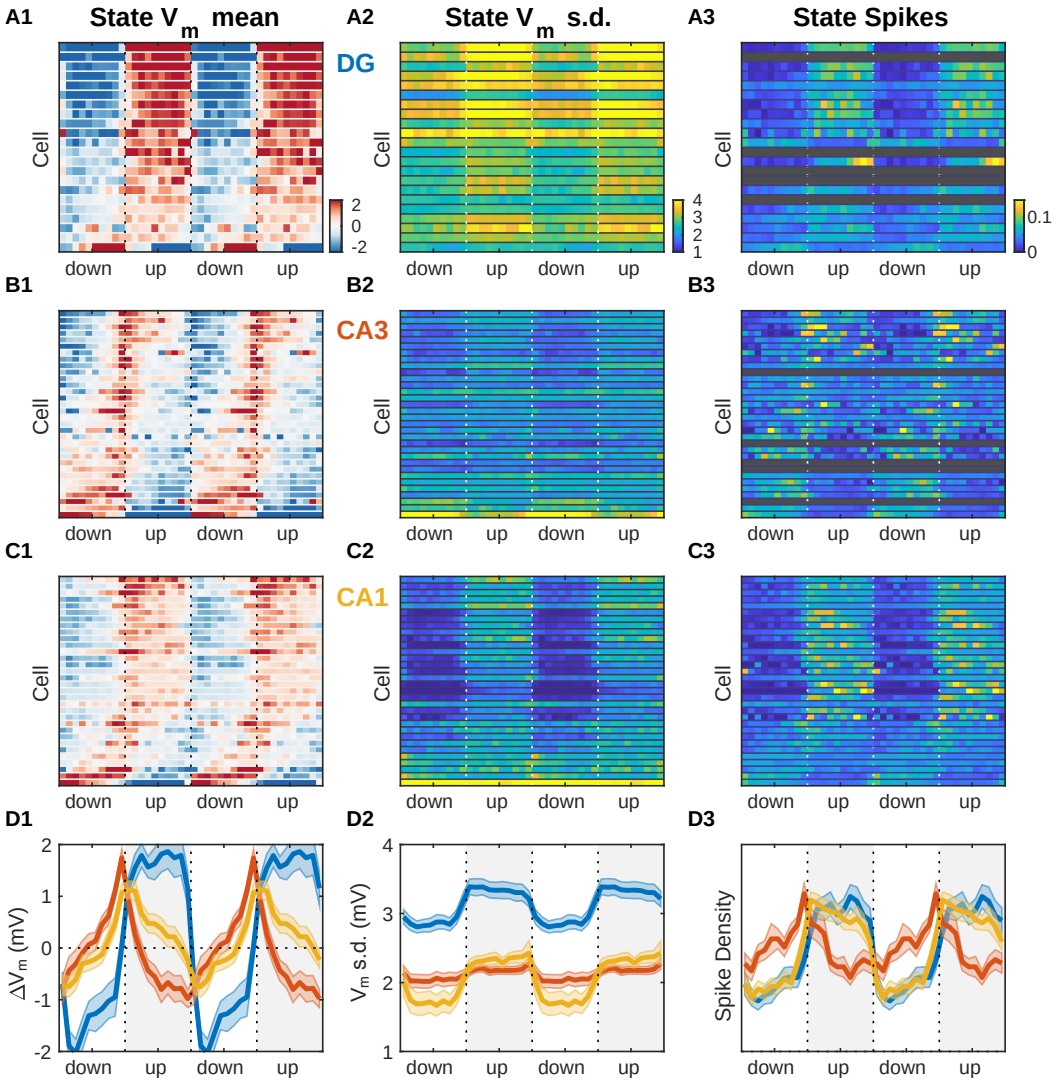

Figure 3.7: **Hippocampal Subfields Exhibit Distinct Activity Profiles over the UDS Cycle. (continued)**
(B) Same as A, but for CA3 pyramidal neurons. Notice that CA3 neurons are maximally hyperpolarized and have lowest firing probability at the end of the UP phase when the rate of ripple occurrence is highest (Figure 3.1E).
(C) Same as A and B, but for CA1 pyramidal neurons.
(D) Area-specific population averages and examples color-coded by brain area.
(D1) Population average Vm means.
(D2) Population average fast Vm component standard deviations.
(D3) Population average spiking probability. Bands around the mean curves show the SEM.

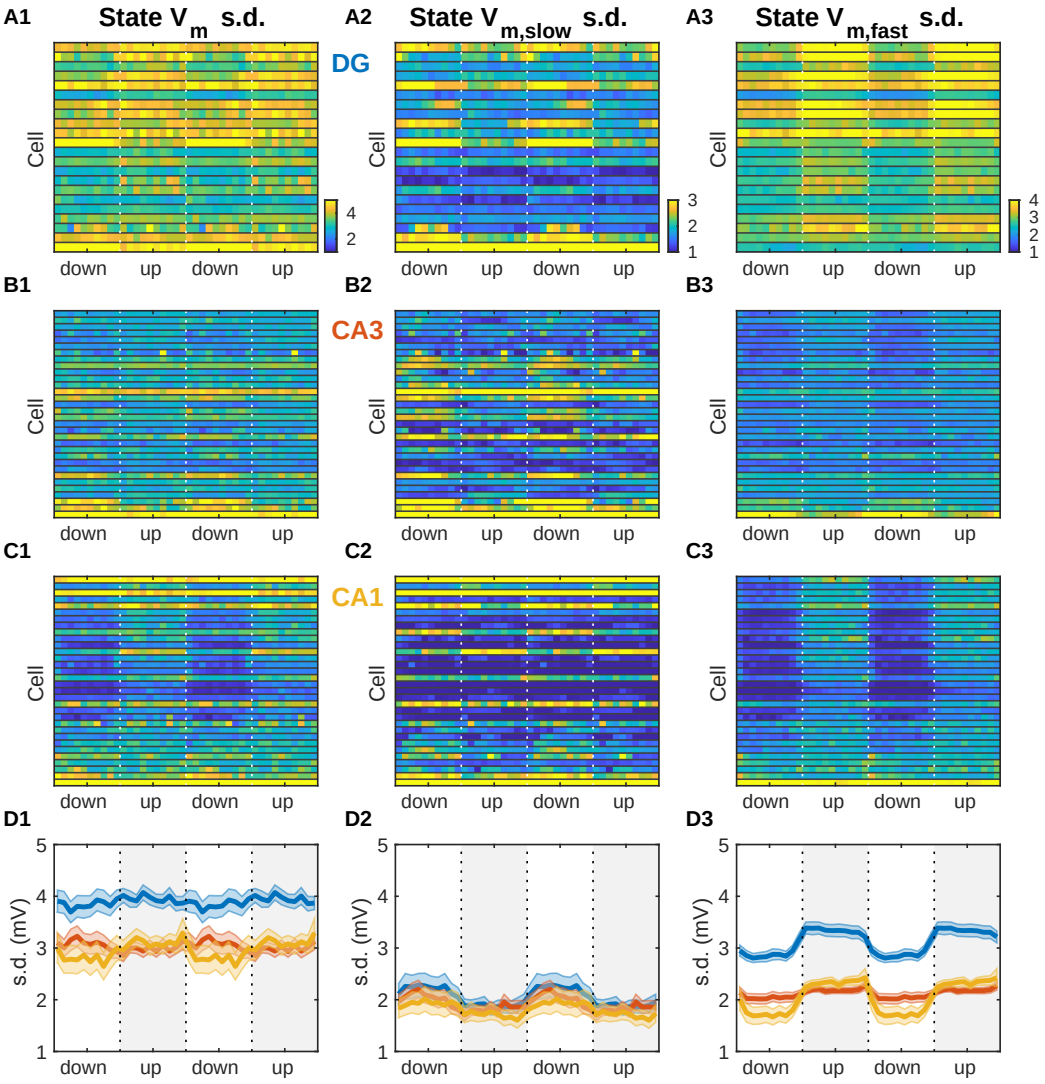

Figure 3.8: **UDS Modulation of Vm fluctuations.**
(A1) Vm standard deviation (s.d.) as a function of UDS phase for DG granule cells. Vertical interrupted lines mark state transitions and in all panels data are replotted over two UDS cycles. Cells are ordered according to UDS rank as in Figure 3.7.
(A2) Slow Vm component s.d. as a function of UDS phase for DG granule cells.
(A3) Fast Vm component s.d. as a function of UDS phase for DG granule cells.
(B) Same as A, but for CA3 pyramidal neurons.
(C) Same as A and B, but for CA1 pyramidal neurons.
(D) Area-specific population averages color-coded by brain area. (D1) Population average Vm s.d. (D2) Population average slow Vm component s.d. (D3) Population average fast Vm component s.d.

3.4 Discussion

Neocortical dynamics during NREM sleep and anesthesia show intrinsic alternation between periods of elevated activity (UP states) and relative quiescence (DOWN states) (R. L. Cowan and C. J. Wilson, 1994; Steriade, McCormick, and Sejnowski, 1993). The entorhinal cortex is the major gateway linking the neocortex with the hippocampal formation and has been shown to exhibit UP and DOWN states (UDS) associated with bimodal membrane potential distributions of EC neurons (Isomura et al., 2006). Despite an absence of bimodality, the subthreshold activity and the spiking of hippocampal neurons is modulated by cortical UDS in a subfield-specific manner both in sleep and under anesthesia (Hahn, Sakmann, and Mehta, 2007; Isomura et al., 2006; Sullivan et al., 2011). We found that DG molecular layer currents exhibit UP-DOWN dynamics indicating that the EC undergoes UDS transitions in quiet wakefulness as well that modulate activity across hippocampal subfields.

Our results regarding UDS modulation in quiet wakefulness are largely consistent with corresponding observations in NREM sleep and under anesthesia, but there were also some notable differences that we highlight below. We observed pronounced modulation of both subthreshold activity and spiking at the DOWN→UP transition in all hippocampal subfields including a 50% increase in the baseline firing rate of CA3 neurons preceding the DOWN→UP transition, consistent with (Isomura et al., 2006) and in contrast to previous reports which found no modulation of CA3 unit activity in sleep/waking immobility (Sullivan et al., 2011) or weak and mixed modulation in anesthetized animals (Hahn, Sakmann, and Mehta, 2007). We also find that awake ripples occur essentially exclusively during the UP state, and not merely with an increased probability relative to the DOWN state (Sullivan et al., 2011). Furthermore, awake ripples occurred throughout the UP state and were not concentrated near the DOWN→UP transitions (Battaglia, Sutherland, and McNaughton, 2004). Finally, in our data the vast majority of CA1 neurons were depolarized on the DOWN→UP transition and had elevated firing rates in the UP state in contrast to previous observations under anesthesia (Hahn, Sakmann, and Mehta, 2007; Isomura et al., 2006).

While the majority of recorded neurons were influenced by UDS, the nature of the modulation is subfield-specific. Granule cells in DG by and large follow the EC inputs and show sustained depolarization and firing rate increase throughout the UP state mirrored by relative hyperpolarization and reduced firing in the DOWN

state. Although CA3 follows DG in the trisynaptic loop, DG activity is more similar to that in CA1 than in CA3. In particular, CA1 pyramidal neurons in CA1 also depolarize and fire more on the DOWN→UP transition, but these responses are more transient than in DG. Consequently, the expected membrane potential across the CA1 population has a triangular wave shape as a function of UDS phase, unlike the square wave shape characteristic of the DG population. This triangular wave shape is almost symmetric with respect to DOWN→UP transition and as a result the Vm conditional means in the UP and DOWN states are very similar, despite the clear Vm modulation by UDS phase. The CA1 population starts depolarizing before the DOWN→UP transition and the DG granule cells. This is reflected in the non-causal transfer model impulse response of CA1 pyramidal cells, which is consistent with the presence of a feedback loop via the CA1→EC connection, but also suggests the presence of another excitatory source, such as CA3, that leads EC activity.

How can activity in CA3 lead given that CA3 is downstream of both the EC and the DG? The majority of CA3 pyramidal neurons are negatively correlated to DG molecular layer currents, which is surprising since CA3 and DG they receive essentially the same excitatory input from layer 2 of the EC as DG granule cells, while the mossy fibers (DG→CA3) form powerful excitatory "detonator" synapses on the proximal dendrites of CA3 pyramidal neurons. Despite this anatomical organization suggesting that CA3 activity should follow that in EC and DG, CA3 pyramidal cells in fact show peak depolarization and elevated firing before the DOWN→UP transition, thus leading both CA1 and DG. Furthermore, a third of the CA3 population is more depolarized in the DOWN state, while the rest exhibit transient depolarization right before the DOWN→UP transition. This is reflected in the negative impulse response of the CA3 transfer model with sustained negative step response. The modulation of the population firing rate in CA3 by UDS is consistent with CA3 being responsible for the CA1 lead over DG activity.

What mechanisms may account for the CA3 behavior? One possibility is that DG and/or EC inputs provide powerful feedforward inhibition to CA3 pyramidal neurons. Indeed mossy fibers (DG→CA3) not only form large mossy terminals on CA3 pyramidal cells but also contact interneurons via filopodial extensions, providing an anatomical substrate for feedforward inhibition (Acsady et al., 1998). The balance between feedforward excitation and inhibition depends on the pattern of granule cell activity: low frequency activation of the mossy fibers results in

powerful slow inhibition of CA3 pyramidal neurons while at higher frequencies an initial depolarization precedes the inhibition (Zucca et al., 2017). Through this mechanism the elevated DG activity in the UP state may induce a concomitant suppression in the majority of CA3 pyramidal neurons during the UP state. As granule cells reduce their firing in the DOWN state, the CA3 circuit is released from the DG-mediated feedforward inhibition and the recurrent CA3 connections may support a sustained increase in population activity. This recurrent excitation is controlled by the strong feedback inhibition present in CA3. The non-causal positive component of the CA3 transfer model impulse response and the timing of CA3 firing relative to the DOWN→UP transition indicate that CA3 may play an important role in ushering the subsequent UP state by providing excitation to EC via CA1. These observations are inconsistent with a feedforward activation of the trisynaptic pathway, suggesting a more complex interplay of intrahippocampal and perforant pathways.

3.5 Methods

Vm decomposition

Spikes were detected by identifying local maxima in the broadband membrane potential with peak prominence of at least 15 mV and width of at most 10 ms. Cells with spike thresholds exceeding -37 mV were considered to be possibly damaged and were therefore excluded from subsequent analyses. The subthreshold membrane potential (Vm) was computed by interpolating the membrane potential over periods with an action potential starting from 3 ms before to 5 ms after the spike peak. The subthreshold Vm signal was then low-pass filtered (Parks-McClellan optimal equiripple FIR filter, 250-350 Hz transition band) and downsampled to 2083 Hz. The Vm signal was decomposed into fast, slow, and drift components as follows. First, the slow Vm component ($V_{m,slow}$) was obtained by median filtering Vm with a 1-second window. Next, the fast Vm component ($V_{m,fast}$) was obtained as the residual Vm after subtraction of $V_{m,slow}$. A drift component ($V_{m,drift}$) was obtained by smoothing $V_{m,slow}$ with a 60-second boxcar kernel. Finally, $V_{m,slow}$ was detrended by subtracting $V_{m,drift}$, which included the resting membrane potential as well as any Vm changes on the timescale of minutes (Figure 3.9). By construction Vm = $V_{m,fast}$ + $V_{m,slow}$ + $V_{m,drift}$ and the components contain different frequency bands of the subthreshold membrane potential.

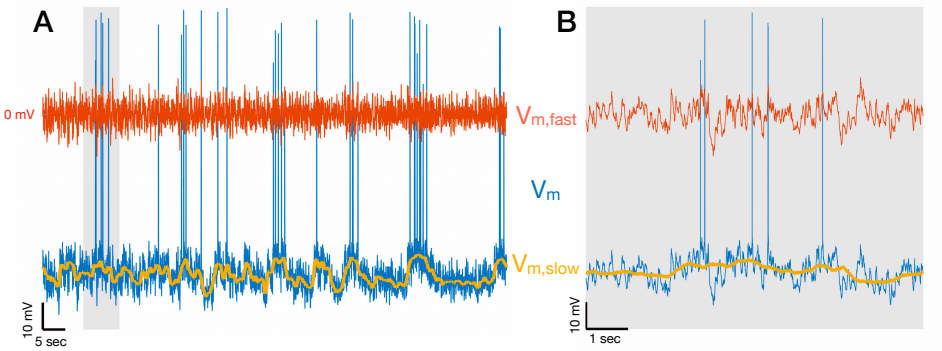

Figure 3.9: **Decomposing Membrane Potential Traces into Slow and Fast Components.**
(A) Membrane potential Vm of a CA3 pyramidal cell (blue) decomposed into slow ($V_{m,slow}$ + $V_{m,drift}$ in yellow) and fast ($V_{m,fast}$ in red) components. After spikes are removed from the membrane potential, $V_{m,slow}$ + $V_{m,drift}$ is obtained by filtering Vm with a median filter with 1 sec window, and $V_{m,fast}$ = Vm - ($V_{m,slow}$ + $V_{m,drift}$). The 1 Hz cutoff frequency for the decomposition is dictated by the fact that Vm is coherent with brain state indicators up to 1 Hz (Figure 3.11B). $V_{m,drift}$ contains the resting membrane potential and Vm changes on the timescale of minutes, so it only adds a DC offset in the panels above. The short segment indicated by the gray vertical bar is shown in (B).

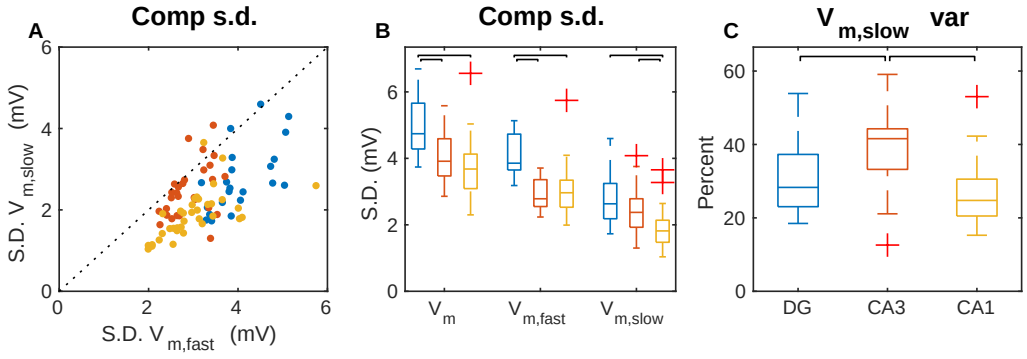

Figure 3.10: **Contributions of Slow and Fast Components to Vm Variability.**
(A) Standard deviations (S.D.) of slow and fast components for each cell (dots) color-coded by subfield. Notice that fast components have more variability than slow components (most dots below the diagonal), but for many CA3 cells (red dots) the variability is comparable between the two components.

Figure 3.10: **(continued)** (B) Component standard deviation (S.D.) grouped by subfield and component. Horizontal bars indicate significant pairwise differences ($p < 0.001$). The Vm of DG cells is most variable both overall and by component. CA1 and CA3 have similar overall and fast component variability, but CA3 has more slow component variability than CA1.
(C) Percentage of total membrane potential variability concentrated in the slow component across hippocampal subfields. CA3 cells have significantly more variability concentrated in the slow component compared to DG and CA1 ($p < 0.01$). The medians for each subfield are DG (28%), CA3 (42%), and CA1 (25%).

Current source density estimation

Local field potentials (LFPs) were recorded from a 32-site silicon probe with 100 μm site spacing positioned so that sites spanned all of neocortex, area CA1, the dentate gyrus, and parts of the thalamus. LFPs were bandpass filtered between 1 Hz and 1 KHz and downsampled to 2083 Hz. Channels with recording artifacts were excluded from the CSD analysis. Laminar current source densities were estimated with 17 μm resolution using a robust version of the one-dimensional inverse CSD spline method (Pettersen et al., 2006). In particular, the forward matrix (relating CSDs to LFPs) was computed as usual, but the inverse matrix (relating LFPs to CSDs) was computed using ridge regression with a regularization parameter set by a cross-validation procedure. The spatial smoothness of the CSD estimate was automatically controlled by the regularization parameter and therefore no further spatial smoothing was applied. The anatomical laminae in CA1 and DG were determined using a combination of histological reconstruction of the probe track, electrophysiological markers (ripples, sharp waves, dentate spikes, etc.), and the CSD covariance structure. DG CSD activity was computed by first averaging the rectified CSD signals from the vertical extent (200 μm) of the suprapyramidal molecular layer of DG (giving the "rectified DG CSD"), then smoothing with a 1-second median filter, and finally converting to a z-score. By construction DG CSD activity only reflects the rate and magnitude of transient synaptic activity and not any slow-varying (< 1 Hz) transmembrane currents.

Transfer model estimation

Linear transfer models were estimated after taking the z-scored DG CSD activity as model input and the slow Vm component of the subthreshold membrane potential of a given cell as output. The finite impulse response (FIR) was estimated from the input-output data using a regularized nonparametric procedure (impulseest in

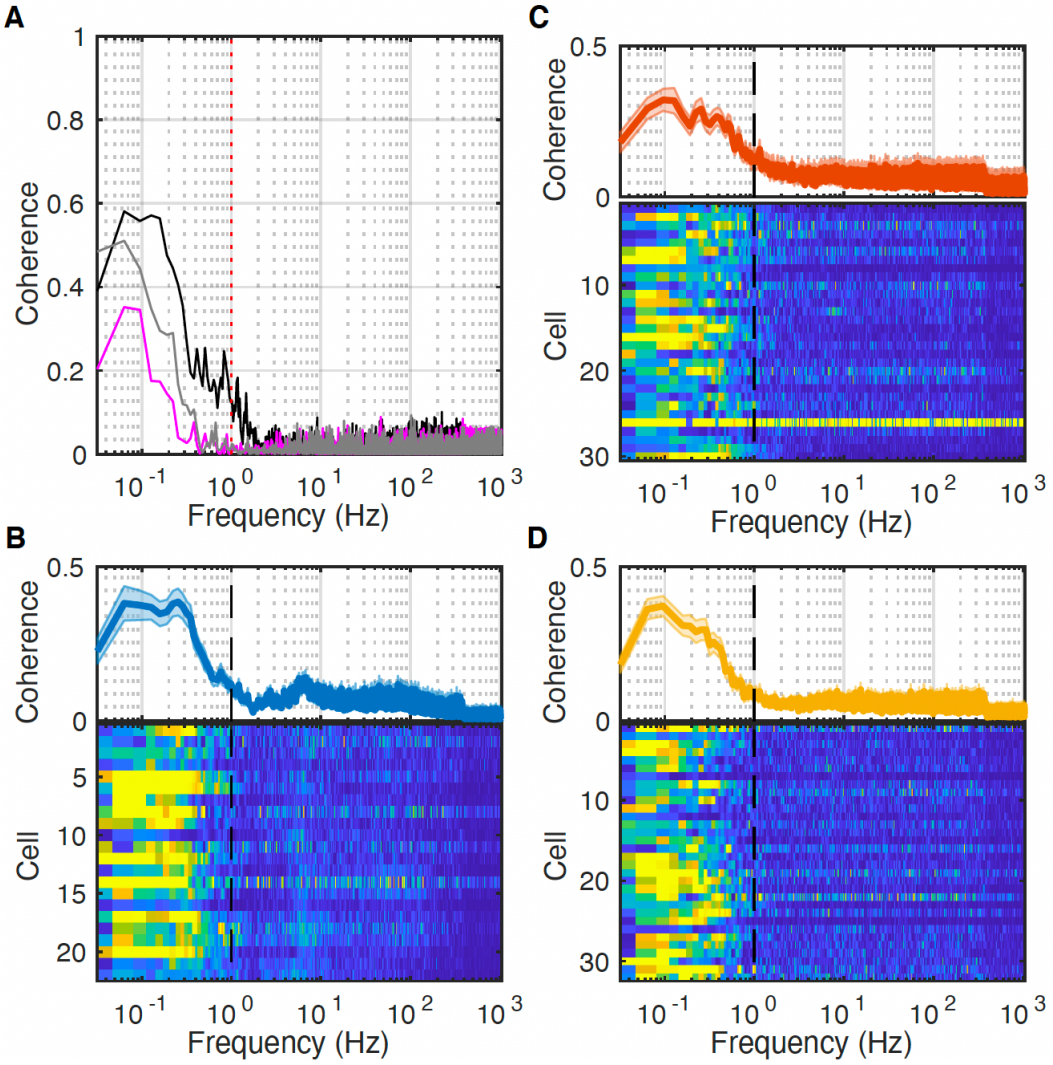

Figure 3.11: **Coherence between rectified DG CSD and Vm.**
(A) Magnitude-squared coherence of subthreshold Vm and rectified DG CSD (black) or pupil diameter (magenta) for the recording in Figure 3.1. Coherence of DG CSD and pupil diameter is shown in gray. Magnitude-squared coherence values range between 0 (uncorrelated) to 1 (perfectly correlated) and measure the strength, not the direction, of the correlation at a given frequency. Notice that the signals are coherent below 1 Hz.
(B) (Bottom) Each row in the pseudocolor image shows the magnitude-squared coherence of subthreshold Vm and rectified DG CSD for a DG cell. (Top) Population average coherence across all DG cells.
(C-D) Same as (B), but for all CA3 (C) and CA1 (D) neurons.

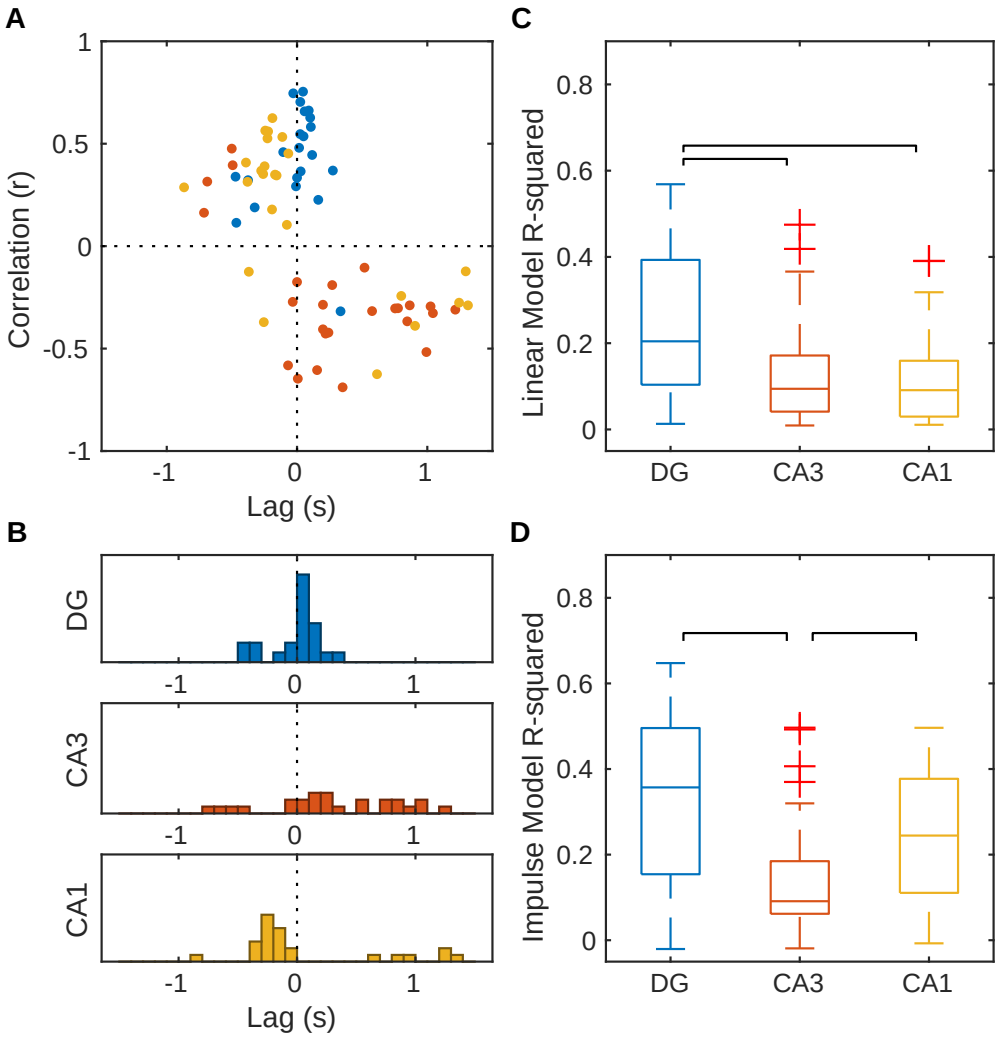

Figure 3.12: **Strength and Direction of the Correlation between Vm Slow Component and DG CSD Activity.**
(A) Lag and amplitude at the absolute peak of the cross-covariance between Vm slow and DG CSD activity. Each dot represents a cell and is color-coded by subfield. Notice that for significantly correlated cells ($p < 0.05$ and $|r| > 0.3$: DG 18/22, CA3 18/32, CA1 16/32) most DG (17/18) and CA1 (13/16) cells have a positive peak correlation, while CA3 cells (15/18) have a negative peak correlation. Notice that the peak correlation for many CA1 cells (14/16) occurs at a negative lag (Vm slow leading DG CSD activity).
(B) Distribution of peak lags for each subfield. Median lags for cells with significant correlation ($p < 0.05$ and $|r| > 0.3$) for each subfield were DG (37 ms), CA3 (296 ms), and CA1 (-225 ms).
(C) Fraction of Vm slow component variance accounted for by its linear correlation to DG CSD activity. The medians are DG (20%), CA3 (9%), and CA1 (9%).
(D) Fraction of Vm slow component variance that can be explained by an impulse response transfer model with DG CSD activity as input. The medians are DG (36%), CA3 (9%), and CA1 (25%).

Matlab System Identification Toolbox with tuned and correlated 'TC' kernel used for regularization) (Chen, Ohlsson, and Ljung, 2012). The input-output data were first downsampled to 20 Hz and the order of the FIR was set to 75, corresponding to 3.6 second duration. The procedure automatically estimated FIR values at negative delays (up to -0.86 sec) and non-zero filter values at negative delays indicated that the slow Vm component led DG CSD activity. Once the impulse responses were estimated the corresponding step responses were simulated by feeding the model with a step input. Low order ARX models were also estimated in a similar manner and led to qualitatively similar results as the FIR models (data not shown).

UP and DOWN state segmentation

UP and DOWN states (UDS) were identified from the z-scored DG molecular layer CSD activity using a hidden Markov model (HMM) (McFarland, Hahn, and Mehta, 2011). First, a binary Gaussian mixture was fit to the distribution of DG CSD values (Figure 3.1C). Next, the mixture components were used to initialize the emission probability distributions of a two state (UP and DOWN) HMM and then the state transition and emission probabilities were estimated from the DG CSD time series data. Finally, the most likely sequence of states given the observed DG CSD time series, downsampled to 4 Hz, were computed with the Viterbi algorithm. The resulting Viterbi path was used to assign a UDS phase to each time point based on its position relative to the nearest UDS transition times. The method was unsupervised and did not require user tuning of any model parameters.

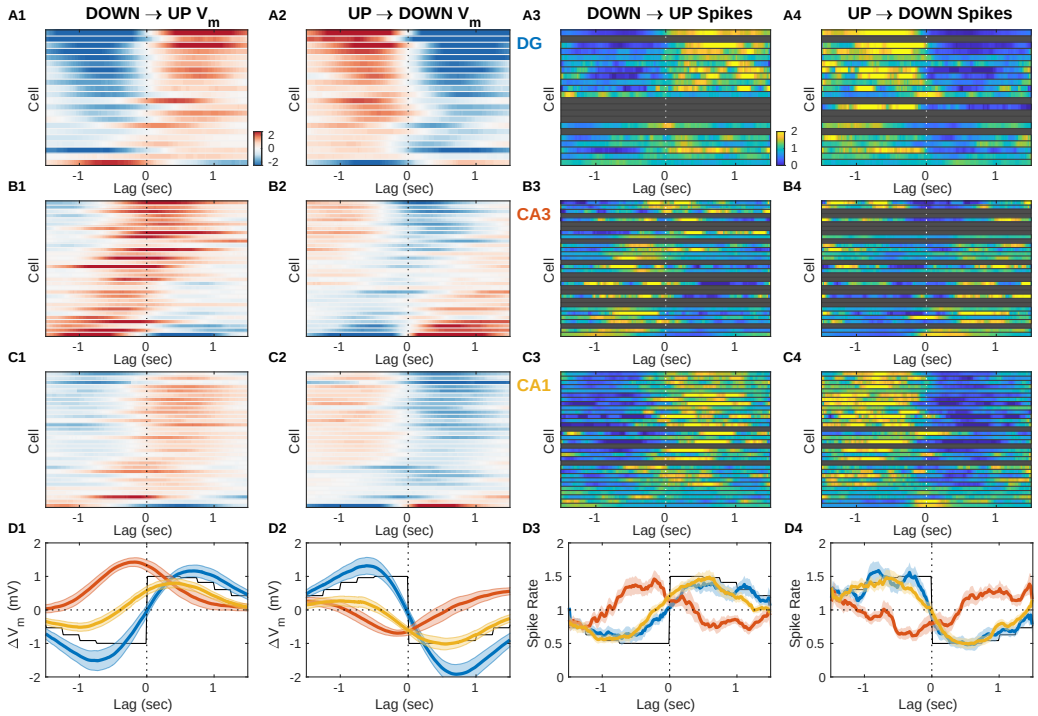

Figure 3.13: **Vm and Spiking Responses to UDS Transitions Reveal Ordering in Subfield Activation.**
(A1) Mean slow Vm component (Vm,slow) triggered on DOWN→UP transitions for each DG granule cell displayed as a row in the pseudocolor image. Cells are ordered by UDS rank as in Figure 3.7. Notice that the Vm of most DG granule cells shifts from hyperpolarized (blue) to depolarized (red) at the UP transition (interrupted vertical line). Color limits in all Vm panels are ±2.5 mV.
(A2) Same as A1, but triggered on UP→DOWN transitions. Notice that in DG the Vm responses to DOWN state transitions are mostly mirror symmetric to the responses to UP transitions.
(A3) Spiking responses to DOWN→UP state transitions for all DG granule cells. The perievent time histogram (PETH) for each neuron is normalized to a baseline rate of 1 Hz, so the colors represent the relative modulation of each cell's baseline firing rate. Notice that firing in the DG is depressed before (blue) and elevated following (yellow) the UP state transition. Grayed out rows correspond to cells with insufficient firing to compute a meaningful PETH.
(A4) Same as A3, but triggered on UP→DOWN transitions. Notice the sharp decrease of firing right at the onset of the DOWN state.
(B) Same as A, but for CA3 pyramidal neurons. Notice that many CA3 cells are already depolarized and have increased firing before the onset of the UP transition.
(C) Same as A and B, but for CA1 pyramidal neurons.
(D) Area-specific population average Vm responses to UP state transitions (D1), DOWN state transitions (D2), and spiking responses to UP transitions (D3) and DOWN transitions (D4). Bands around the mean curves show the standard error of the mean. Black traces show the average state at each lag with the DOWN and UP states represented by -1 and 1 in D1-2; 0.5 and 1.5 in D3-4.

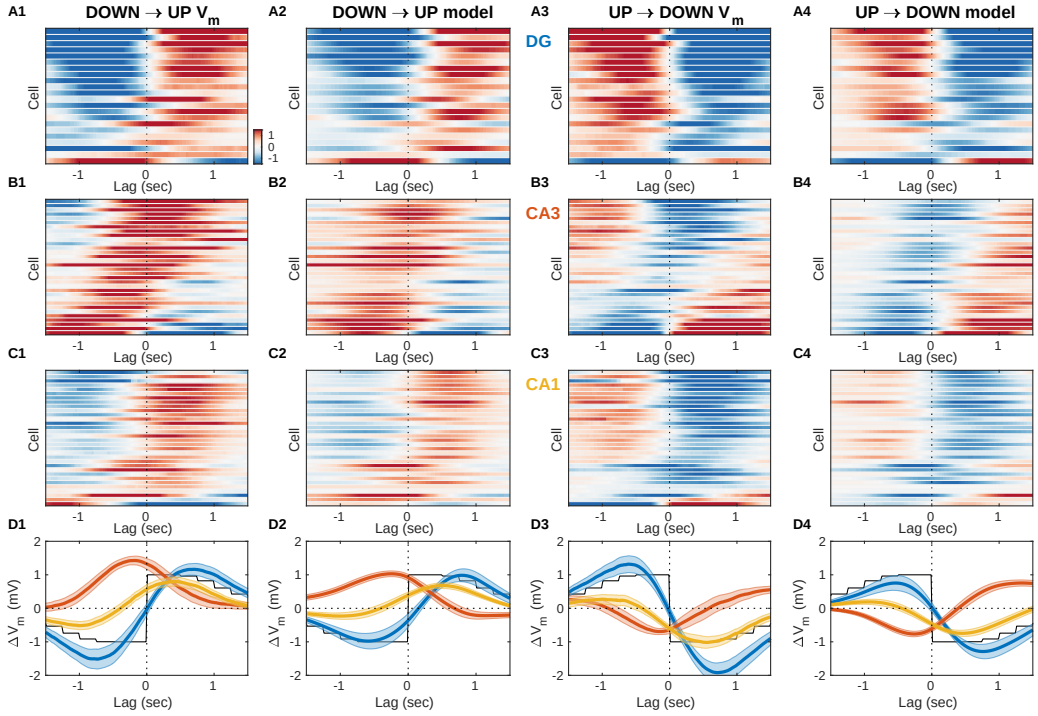

Figure 3.14: **Vm and Transfer Model Responses at UP and DOWN State Transitions.**
(A1-D1) Observed Vm responses at DOWN→UP transitions. Data are replotted from Figure 3.13 for comparison, but reordered according to the UP Vm responses. All other panels follow this same ordering. In all panels cells are ordered by UDS rank is in Figure 3.7.
(A2-D2) Transfer model responses at DOWN→UP transitions simulated from the observed DG CSD activitymagnitude.
(A3-D3) Observed Vm responses at UP→DOWN transitions (replotted from Figure 3.13 for comparison).
(A4-D4) Transfer model responses at UP→DOWN transitions simulated from the observed DG CSD activitymagnitude.
Bands around the mean curves show the SEM.

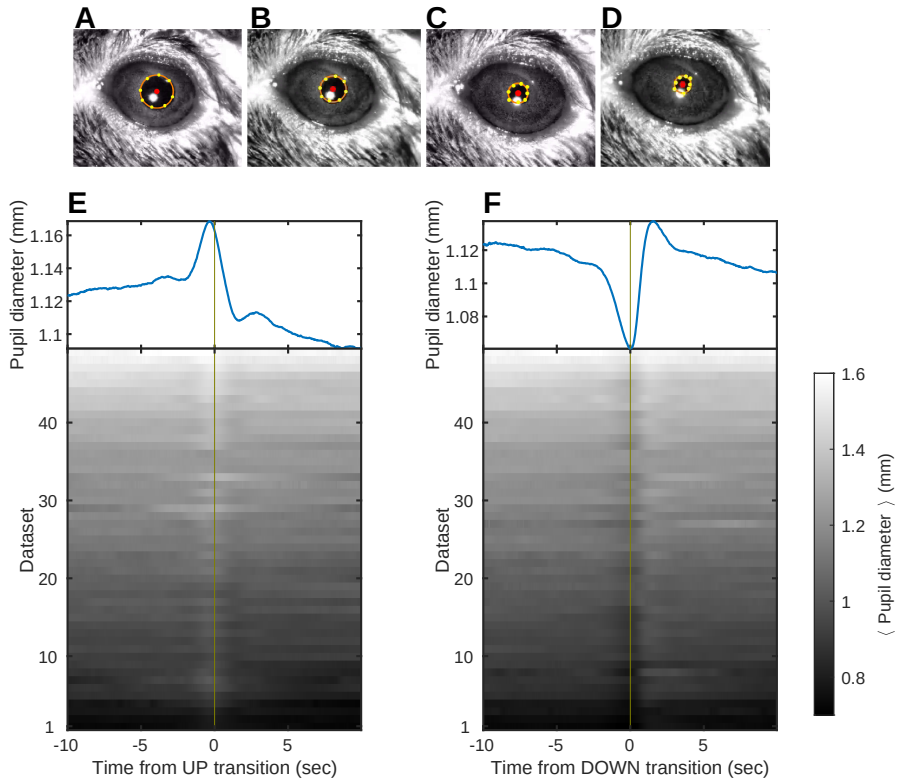

Figure 3.15: **Pupil Diameter around UP and DOWN transitions.**
(A-D) Examples of pupil tracking. Eight points around the pupil edge were labeled in a subset of frames, and in the remaining frames corresponding points were extracted with DeepLabCut (yellow). The pupil diameter was estimated by fitting a circle (orange) to the extracted points.
(E-F) Mean pupil diameter per dataset (bottom) and average across datasets (top) centered on DOWN→UP (E) and UP→DOWN (F) transitions. Notice that the pupil starts dilating at the onset of the DOWN state (F) and is in the process of constricting at the onset of the UP state (E).

Pupil Analysis

Pupil videos were analyzed using DeepLabCut (Mathis et al., 2018). A subset of frames were manually labeled with 8 points around the pupil and these points were subsequently extracted with DeepLabCut for the remaining frames. A core set of points with likelihood > 0.7 was detected for each frame and a circle was fit using

the Taubin SVD-based method for frames with more than 3 core points (Taubin, 1991). Blinks were detected as abrupt drops in likelihood across the detected points. Datasets with mean likelihood across detected points above 0.95 and with more than 97% valid frames were selected for analysis. Proper extraction of pupil diameter and blinks was confirmed by visual inspection.

Chapter 4

INHIBITION IS THE HALLMARK OF CA3 INTRACELLULAR DYNAMICS AROUND AWAKE RIPPLES

Ripples are believed to be the product of excitatory buildup in the recurrent CA3 network, culminating in a population burst that drives CA1 spiking organized by the transient ripple oscillation (Buzsáki, 1986; Miles and Wong, 1983; Stark et al., 2014; Traub and Miles, 1991).This suggests that CA3 neurons should get progressively depolarized and come closer to firing threshold through the course of the ripple buildup. Separate from the buildup itself, the processes controlling ripple initiation and termination are not fully understood. *In vitro* experiments indicate that ripples are initiated once stochastic fluctuations in the population firing rate of CA3 pyramidal cells exceed a threshold level (Prida et al., 2006; Schlingloff et al., 2014), implying that an increase in the firing of CA3 neurons should result in a corresponding increase in the rate of ripple occurrence. Recent *in vitro* studies have also emphasized the importance of inhibitory neurons in ripple initiation (Bazelot, Teleńczuk, and Miles, 2016; Ellender et al., 2010; Schlingloff et al., 2014), while other studies suggested that area CA2 and a special class of CA3 cells play a key role in ripple initiation (Hunt et al., 2018; Oliva et al., 2016). Furthermore, there is growing evidence that the functional role of ripples as well as the mechanism of their initiation may differ across the awake and sleep states (Middleton and McHugh, 2020; Oliva et al., 2016; Roumis and Frank, 2015; Tang and Jadhav, 2019). Whole cell recordings in awake animals have opened a window to understanding the interplay between collective network activity and Vm dynamics of hippocampal neurons which can reveal the nature and timing of synaptic inputs and subthreshold changes that are invisible to extracellular recordings. While recent efforts have examined the Vm of CA1 neurons around ripples (English et al., 2014; Hulse, Moreaux, et al., 2016) and the Vm modulation by brain state across hippocampal subfields (Hulse, Lubenov, and Siapas, 2017; Malezieux, Kees, and Mulle, 2020), the subthreshold dynamics of CA3 pyramidal cells around ripples and the impact of cortical inputs on Vm behavior in CA3 remain unknown.

Below, we focus on characterizing how brain state is reflected in slow Vm trends around ripples. Then, we analyze ripple triggered modulation of fast Vm fluctuations which reveals a prevalence of inhibition in CA3 which grows through the ripple

buildup. In contrast DG and CA1 neurons exhibit transient depolarization not only after ripple onset but also 100 ms earlier.

4.1 Inhibition Dominates CA3 Subthreshold Behavior Near Awake Ripples

It has long been appreciated that awake ripples preferentially occur during periods of quiet wakefulness and LIA. Furthermore, here we showed that when quiet wakefulness is segmented into periods of UP and DOWN states, essentially all ripples occur in the EC UP state (Figure 3.1E). The prevailing view is that ripples are the result of self-organized population bursts of activity that build within the recurrent CA3 network and then are transmitted to and further patterned by the CA1 network, where the ripple oscillation itself is readily observable in the local field near the pyramidal cell layer (Figure 3.1A) (Miles and Wong, 1983; Buzsáki, 1986; Traub and Miles, 1991; Stark et al., 2014). How do neurons across the different hippocampal subfields participate in this process? To address this question we detected ripple onset times from the CA1 local field near the pyramidal cell layer and determined the ripple-triggered average (RTA) Vm and firing rate modulation for each recorded cell (Figure 4.1). Since the RTA of the Vm is the sum of the RTAs of the fast and slow Vm components, we determined these average responses separately for each cell and component (Figure 4.1A1-D1, 4.1A3-D3). The RTAs of the slow Vm component showed pronounced depolarization in DG with a peak before the ripple onset, a hyperpolarization in CA3 with a trough following the ripple onset, and mixed responses in CA1 (Figure 4.1A1-D1). Since ripples occurred exclusively during the UP state and the slow Vm component of hippocampal neurons was strongly influenced by state, we hypothesized that the RTA slow Vm response depended strongly on the pattern of EC input and how each cell was impacted by it. We therefore simulated the slow Vm component for each cell using the linear transfer models we had estimated (Figure 3.5) and computed the ripple-triggered average of the simulated slow Vm response (Figure 4.1A2-D2). The RTAs of the observed and simulated slow Vm components showed good qualitative agreement indicating that on the timescale of seconds Vm trends near ripples are strongly influenced by the pattern of EC UDS transitions.

In contrast, the mean of the fast Vm component is very weakly influenced by state and therefore its RTA should reflect synaptic activity consistently timed with respect to the ripple onset. Consistent with previous studies, we found that the fast RTA Vm waveform for most CA1 pyramidal neurons had a sharp prominent peak following the ripple onset, followed by a steep return to baseline or hyperpolarization within

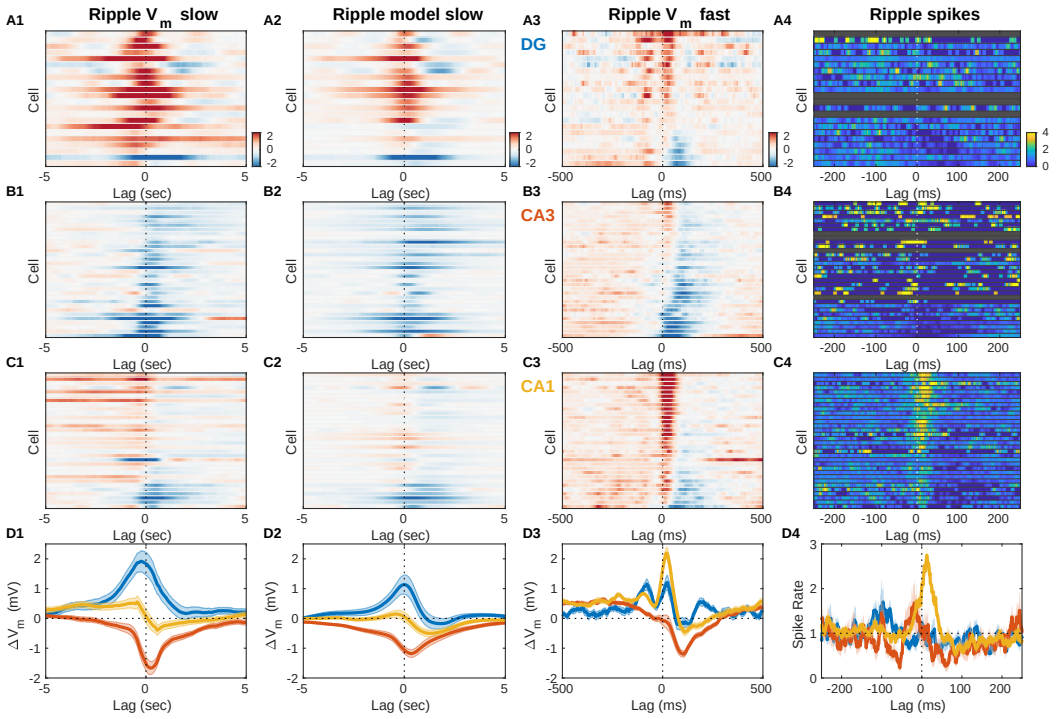

Figure 4.1: **Inhibition Marks Slow and Fast Vm Responses near Ripples in CA3, Unlike DG or CA1.**
(A1) Mean slow Vm component triggered on ripple onset for each DG granule cell displayed as a row in the pseudocolor image. Interrupted vertical line marks ripple onset.
(A2) Transfer model predicted ripple-triggered slow Vm component as in A1.
(A3) Mean fast Vm components triggered on ripple onset and displayed as in A1. Notice the two depolarizing peaks at -100 ms and right after ripple onset. Cells in panels A1-3 are ordered by the first principal component coefficient of the A3 image matrix (RTA rank).
(A4) Spiking response to ripple onset for DG cells normalized by baseline firing rate.
(B) Same as A, but for CA3 pyramidal neurons. Notice the prominent hyperpolarization for most CA3 neurons present in both the slow and fast Vm component responses.
(C) Same as A and B, but for CA1 pyramidal neurons. Notice the prominent depolarization for most CA1 neurons.
(D) Area-specific population average slow Vm response (D1), transfer model predicted slow Vm responses (D2), fast Vm response (D3), and spiking response (D4) color-coded by brain area. Bands around the mean curves show the SEM. Notice that modulation by UDS accounts for the shape of the ripple-triggered Vm response on the timescale of seconds (compare D1 and D2).

a 100 ms (Figure 4.1C3) (Hulse et al. 2016). This behavior was mirrored in the firing rate modulation of CA1 cells (Figure 4.1D3) and is consistent with the notion that CA1 exhibits a highly synchronous population burst associated with ripple oscillations.

Since the population event in CA1 is presumably due to a self-organized population burst in CA3, one might expect that the fast RTA waveforms in CA3 should resemble those in CA1, but this was not the case (Figure 4.1B3). While a minority CA3 neurons (9/32) exhibited a small depolarizing peak near the ripple-onset, the most consistent feature of the fast RTA Vm waveform in CA3 was the prominent hyperpolarization that reached a trough roughly 100 ms following ripple onset and recovered within 300 ms. The population average response shows that the decrease in Vm had begun as early as 150 ms prior to the ripple onset (Figure 4.1D3). Similarly, while several CA3 neurons showed an increase in firing rate just prior to the ripple onset, about a third of the CA3 population exhibited a reduction in firing rate before and especially following the ripple onset (Figure 4.1B4, 4.1D4). These data demonstrate that extensive inhibition, rather than excitation, is the hallmark of CA3 subthreshold activity before and after ripple bursts. Further analysis of the CA3 cells with a depolarizing peak near the ripple onset (9/32 cells) revealed that they do not have significantly different resting Vm, spike threshold, burst index, or spikes per burst compared to the rest of the CA3 population (data not shown). However, these CA3 cells had lower firing probability in the DOWN state and lower overall firing rates than the remaining CA3 population. It is worth noting that most neurons, even with hyperpolarizing average response, experienced depolarization and firing during a subset of ripples, consistent with a sparse activation of CA3 during ripples (Figure 4.2).

Finally, while the dentate gyrus has not been traditionally considered to be instrumental to the process of ripple generation, the fast RTA Vm waveforms of granule cells showed clear modulation with about half of the population exhibiting a depolarization peak following ripple onset with a similar time course to that seen in CA1 (Figure 4.1A3). Interestingly, about half of DG granule cells also showed another depolarization peak occurring 100 ms prior to ripple onset (Figure 4.1A3, 4.1D3). Upon closer examination a similarly timed depolarizing peak could be seen in the CA1 response prior to ripple onset, although of much smaller magnitude in comparison to the post-ripple depolarization. Similarly, a sharp wave of smaller amplitude is also consistently observed 100 ms before ripple onset (Hulse, Moreaux, et al.,

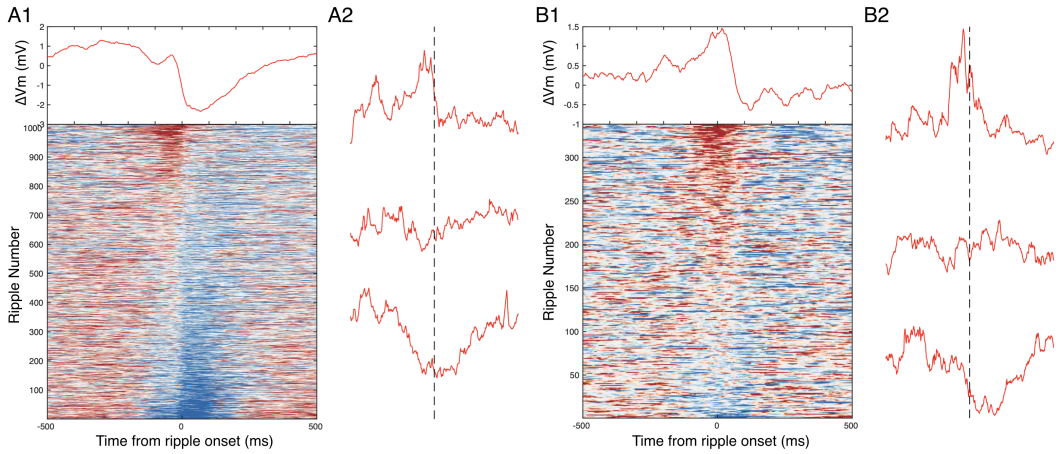

Figure 4.2: **Membrane Potential Dynamics of CA3 Pyramidal Neuron during Single Ripples.**
(A1) (Top) Mean fast Vm component of one example CA3 pyramidal cell triggered on ripple onset. (Bottom) Fast Vm components of CA3 pyramidal cell triggered on ripples. Each row corresponds to a single ripple. Notice that, even with hyperpolarizing average response, the neuron experienced depolarization during a subset of ripples.
(A2) Examples of fast Vm component triggered on ripple onset chosen from A1 Bottom. Vertical dashed line mark the time of the ripple onset. Notice the variable fast Vm activities.
(B1) Same as A1, but for the neuron with depolarizing average response. Notice that, even with depolarizing average response, the neuron experienced hyperpolarization during a subset of ripples.
(B2) Same as A2, but for the neuron with depolarizing average response. Notice the variable fast Vm activities.

2016).

Since ripples can occur in close succession at intervals close to 100 ms, we wondered if such ripple bursts could contribute to the observed pre-ripple depolarization. To test this hypothesis we compared the fast RTA Vm aligned to the onset of isolated single ripples with that the average Vm aligned to the onset of ripple doublets. The pre-ripple depolarization in DG and CA1 was similar for isolated ripples and ripple doublets arguing against the hypothesis that pre-ripple responses were due to a reflection of ripple bursts (Figure 4.3). These data indicate that DG should not be viewed as a passive bystander in the awake ripple generation process and that the ripple proper is preceded by coordinated activity not only in CA3, but also in CA1 and DG.

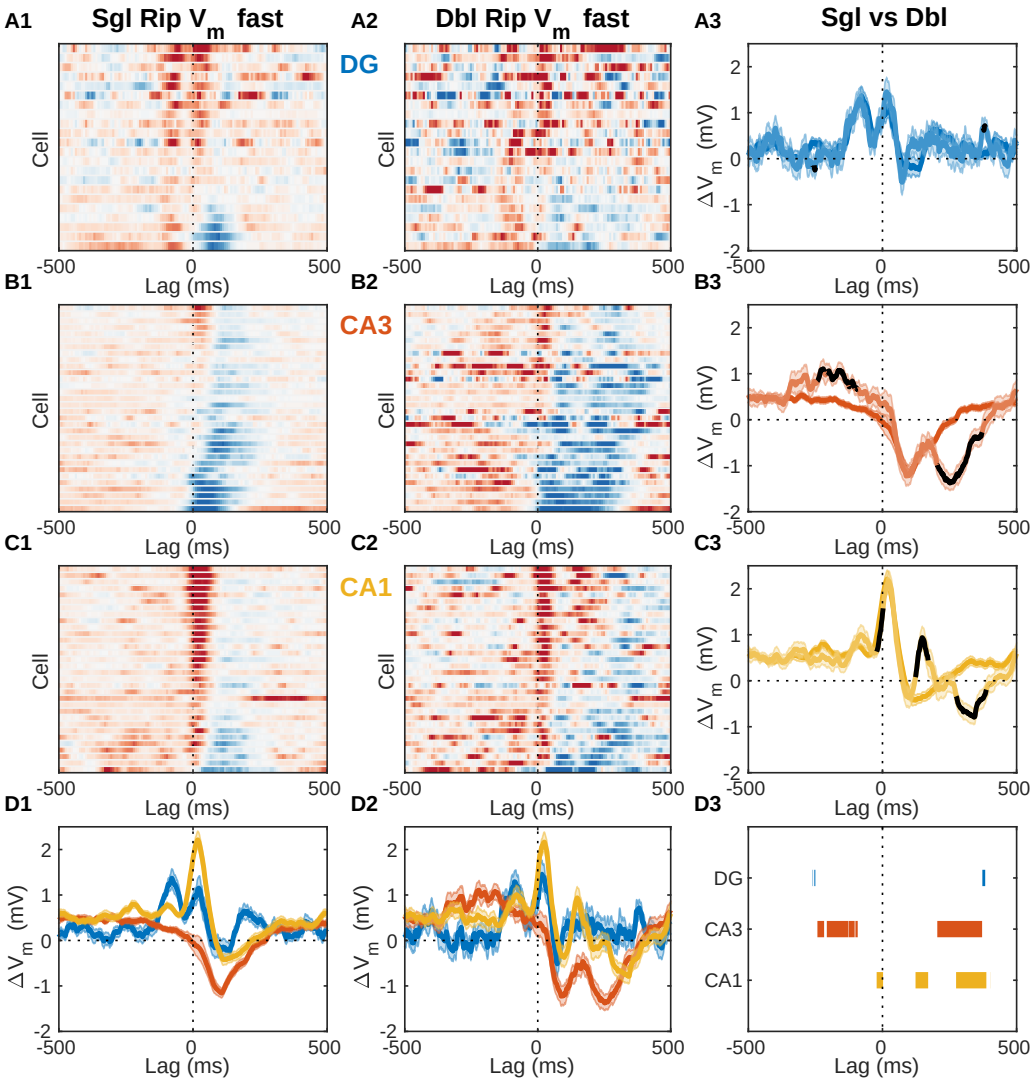

Figure 4.3: **Subthreshold Ripple Modulation around Isolated Ripples and Ripple Doublets.**
(A1) Mean fast Vm components of DG granule cells triggered on isolated ripples (no ripples occurring within 250 ms from ripple onset). (A2) Mean fast Vm components of DG granule cells triggered on the onset of first ripple of a ripple doublets (with a second ripple occurring within 250 ms from the start of the first).

4.2 Feedback Inhibition Hyperpolarizes CA3 Neurons During Ripples

What circuit mechanisms may be responsible for the observed subthreshold activity around ripples? Since CA3 is considered to play a key role in the process of ripple generation, we reasoned that influences on subthreshold activity originating in CA3 should scale in proportion to the CA3 population burst size. We inferred this size indirectly from the amplitude of the ripple-associated sharp wave in stratum

Figure 4.3: **(continued)**
(A3) Comparison of the DG population averages for isolated ripples (darker hue) vs. ripple doublets (lighter hue). Significant differences are highlighted in black. Notice that DG responses are almost identical and the depolarization peak at -100 ms is present before the onset of both isolated ripples and ripple doublets.
(B) Same as A but for CA3 pyramidal neurons. Notice that while there is significantly more pronounced depolarization preceding ripple doublets, the CA3 response through the course of the first ripple in the doublet matches that seen during isolated ripples. Responses diverge again 200 ms following the onset of the first ripple and an additional hyperpolarization trough is evident at 250 ms due to the second ripple.
(C) Same as A,B but for CA1 pyramidal neurons. Notice that the secondary depolarization peak in CA1 in response to ripple doublets occurs at 150 ms, halfway between the two hyperpolarization troughs seen in CA3.
(D) Area-specific population average responses to isolated ripples (D1) and ripple doublets (D2). (D3) Horizontal bars mark the onset and duration of significant differences between responses to isolated ripples and ripple doublets.

radiatum of CA1 or equivalently by the magnitude of the underlying synaptic current due to Schaffer collateral activation (Mizunuma et al., 2014). We then divided the ripples from each recording session in two halves, big and small, depending on whether they were associated with above-median or below-median CA3 burst size. Finally, we computed the fast RTA Vm waveform separately for big and small CA3 events and compared the results (Figure 4.4). The size of the CA3 burst had little effect on the DG RTA waveform, apart from a slight increase in hyperpolarization about 100 ms following ripple onset that was associated with the bigger events (Figure 4.4A1-A3). In contrast, subthreshold activity in CA3 clearly reflected the size of the CA3 population event (Figure 4.4B1-B3). Larger CA3 events were associated with more sustained depolarization up to 300 ms prior to the ripple onset and deeper hyperpolarization following (Figure 4.4B3). In CA1, bigger CA3 events were associated with slightly more depolarization up to 250 ms prior to the ripple onset and during the post-ripple peak, but the most notable difference was the increased hyperpolarization about 100 ms following the ripple onset (Figure 4.4C1-C3). These data indicate that feedback inhibition within CA3 is most likely responsible for the subthreshold hyperpolarization seen in the fast Vm component around ripples in CA3. Consistent with our previous study, it also suggests that feedforward inhibition from CA3 to CA1 may play an important role in controlling the population event size in CA1 and may contribute to the post-ripple hyperpolarization (Hulse, Moreaux, et al., 2016).

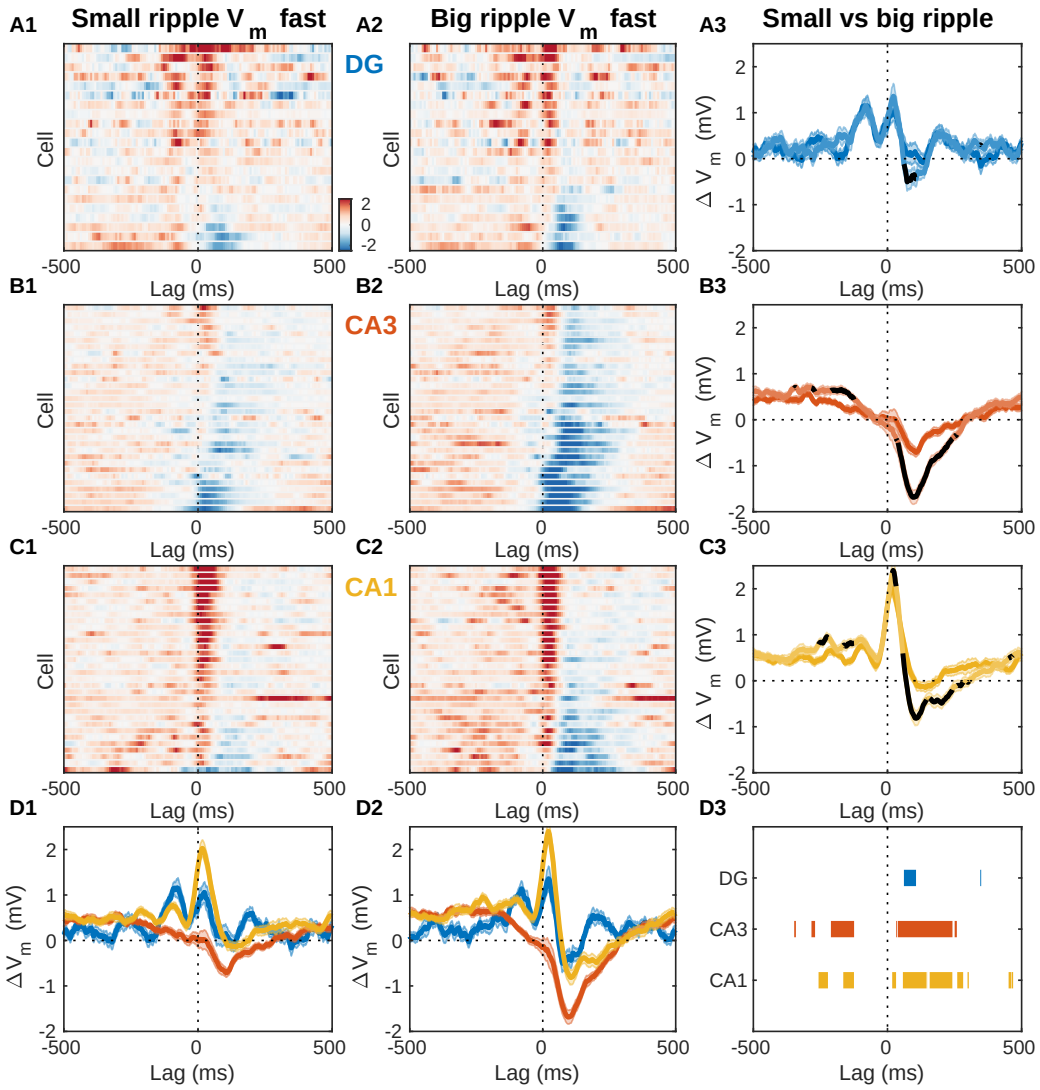

Figure 4.4: **Fast Vm Inhibitory Responses to Ripples Scale with CA3 Population Burst Size.**
(A1) Mean fast Vm components of DG granule cells triggered on ripples with small (below average) sharp-wave (SPW) amplitudes.
(A2) Same as A1, but for ripples with big (above average) SPW amplitudes.
(A3) Comparison of the DG population average response to small and big SPW ripples. Bands around the mean curves show the SEM. Responses to big ripples are shown in darker blue and overlap the responses to small ripples for most time lags. For significant differences the responses to big ripples are highlighted in black (paired t-test, $p<0.01$).
(B) Same as A, but for CA3 pyramidal neurons.
(C) Same as A and B, but for CA1 pyramidal neurons.
(D) Area-specific population average responses to small (D1) and big (D2) SPW ripples. Bands around the mean curves show the SEM. (D3) Horizontal bars mark the onset and duration of significant differences between responses to small and big SPW ripples within each area (paired t-test, $p<0.01$).

4.3 Discussion

The recurrent circuit of CA3 has long been hypothesized to function as an autoassociative memory network (Marr, 1971) and to support the buildup of population activity underlying the ripple generation process (Buzsáki, 2015). Indeed, acute silencing of Schaffer collaterals during wakefulness abolishes ripples (Davoudi and Foster, 2019; Yamamoto and Tonegawa, 2017). While the membrane potential of CA1 pyramidal neurons near ripples has been shown to exhibit a gradual ramping and a transient depolarization followed by a prolonged inhibition (Hulse, Moreaux, et al., 2016), the subthreshold dynamics of DG granule cells and CA3 pyramidal neurons near ripples in awake animals had not been fully characterized.

We observed that the ripple-triggered membrane potential of hippocampal neurons is modulated on a timescale of seconds, with DG granule cells showing depolarization, CA3 pyramidal neurons hyperpolarization, and CA1 cells exhibiting weaker modulation. Since ripples occur almost exclusively in the UP state and the slow Vm dynamics of hippocampal cells are modulated by UDS in a subfield-specific fashion, we hypothesized and confirmed that the slow Vm responses near ripples can be qualitatively accounted for by the UDS influence on hippocampal cells.

How does UDS influence hippocampal network excitability? It has been proposed that during NREM sleep hippocampal dynamics exhibit a stable, but excitable quiescent state, such that activity fluctuations can produce a transient population excitation representing a ripple (Levenstein, Buzsáki, and Rinzel, 2019). Our data indicate that in quiet wakefulness UDS modify hippocampal network excitability because no ripples are produced in the DOWN state. We illustrate this behavior in a mean firing rate model in the framework described in (Levenstein, Buzsáki, and Rinzel, 2019), featuring two (EC and CA3) adapting recurrent neural populations (Figure 3.14). In the model the EC population influences CA3 activity by providing a net inhibitory input as well as by modulating the strength of the CA3 recurrent excitation (Figure 4.5). In the real circuit the latter influence may be due to UDS-dependent changes in neuromodulatory inputs, such as cholinergic tone, as exhibited, for example, by pedunculopontine cholinergic neurons (Mena-Segovia et al., 2008). The majority of the cholinergic input to the hippocampus originates in the medial septum and optogenetic stimulation of septal ChAT-positive neurons suppresses ripple generation (Hunt et al., 2018; Vandecasteele et al., 2014). Acetylcholine is known to inhibit the efficacy of recurrent synaptic transmission in CA3 by acting on presynaptic muscarinic receptors in the associational–commissural fiber

system (Hasselmo, Schnell, and Barkai, 1995; Hasselmo and Schnell, 1994; Vogt and Regehr, 2001) and cholinergic tone is presumably at its lowest during ripple generation in the EC UP state. Thus the efficacy of CA3 recurrent connections together with dentate and entorhinal input to CA3 and the associated feedforward inhibition can act as bifurcation parameters for the CA3 network dynamics that change network excitability thereby preventing ripple occurrence during the cortical DOWN state (Figure 4.5E-F). This is counterintuitive because many CA3 neurons are more active and depolarized in the DOWN state or near the DOWN→UP transition and so, according to the stochastic-refractory model of ripple initiation (Schlingloff et al., 2014) the rate of ripple occurrence should coincide with the modulation of CA3 activity by UDS, which is contradicted by the fact that ripples occur in the UP state. In our model, CA3 network excitability is shown to be restricted to the EC UP state when the mean CA3 rate is lower compared to the DOWN state (Figure 4.5B-C). This is possible because of the push-pull influences of the net inhibitory input which lowers CA3 network excitability, and the CA3 recurrent strength potentiation which increases it. Hence, in the UP state the CA3 network is inhibited but excitable, while in the DOWN state it is disinhibited but not excitable (Figure 4.5).

These data suggest that increased inhibition in CA3 may be a prerequisite for ripple initiation. This is consistent with *in vitro* work showing that reducing $GABA_A$-mediated inhibition in hippocampal slices abolishes spontaneously occurring sharp wave-ripple events in CA3 (Bazelot, Teleńczuk, and Miles, 2016; Ellender et al., 2010; Schlingloff et al., 2014). The relative hyperpolarization in CA3 during the UP state may reflect the role of certain local (Katona et al., 2014; Viney et al., 2013) or long-range projecting interneurons (Basu et al., 2016; Unal et al., 2018) in suppressing the initiation of ripples. According to one view, ripple generation may be the result of disinhibition, however our data does not offer clear evidence for widespread disinhibition in CA3 preceding the population burst (Evangelista et al., 2020). Importantly, ripple generation by disinhibition does not account for the lack of ripples in the DOWN state, despite the elevated neuronal activity in CA3. Its origin notwithstanding, membrane hyperpolarization in CA3 may influence ripple initiation by affecting voltage-gated conductances and thereby changing the excitability of CA3 neurons to make them more likely to fire or burst in response to transient depolarizing input. Changes in inhibition across the CA3 network may shift the region of ripple initiation, allowing for reactivation of diverse memory traces stored within the CA3 network.

On a faster timescale, the average Vm responses near ripples reveal two consistent features. First, the majority of CA3 neurons exhibit a brief (300 ms) hyperpolarization locked to the ripple onset in addition to the broad (3 sec) UDS-mediated hyperpolarization. This brief hyperpolarization grows with the size of the CA3 population burst, quantified by the associated sharp wave amplitude, therefore pointing to feedback inhibition as its source. This suggests that feedback inhibition is a consistent feature of the buildup process in CA3. This inhibition likely arises from several classes of interneurons that have been shown to exhibit elevated firing around ripples in both CA3 and CA1 (Klausberger et al., 2003; Somogyi et al., 2014; Tukker et al., 2013). However, the distinct Vm responses we observed around ripples indicate that inhibition is tuned differently in CA3 and CA1. In particular, in CA1 inhibition imposes oscillatory patterning on the Vm that rides on a wave of depolarization, while in CA3 inhibition summates to produce a net hyperpolarization. In both areas however, fast fluctuations in the membrane potential persist throughout the ripple period allowing CA3 neurons to fire despite the net hyperpolarization. These results suggest that the relative gain of feedback inhibition is greater than that of recurrent excitation for the majority of the CA3 neurons and hence the population burst can only build up by recruiting the CA3 neurons most strongly connected to a sparse active subset. This may reflect a winner-take-all mechanism for controlling both the sparsity and the specificity of the neuronal sequences activated in CA3 during a ripple. The growing inhibition during the course of a ripple also provides a mechanism for ripple termination.

Second, DG granule cells exhibit two transient depolarizations of comparable amplitude 100 ms before and immediately after the ripple onset. Similarly timed features are present in the Vm of CA1 pyramidal neurons, albeit the pre-ripple depolarization is significantly smaller than the post-ripple one. In CA1, both depolarizations are associated with sharp waves of proportional magnitudes in stratum radiatum (Figure 4A in (Hulse, Moreaux, et al., 2016)), implicating CA3 as the source for both. The DG activation is consistent with the presence of a backprojection from CA3 to DG (Scharfman, 2007; Szabo et al., 2017) and can influence ripple-associated CA3 activity, consistent with previous lesion studies (Sasaki et al., 2018). These results indicate a long and orchestrated ripple initiation process in the awake state, extending beyond the roughly 50 ms period of excitatory activity buildup that proceeds ripples *in vitro* (Schlingloff et al., 2014).

While there are consistent features within each subfield with respect to UDS and

ripple modulation, there is also variability of responses across cells. The resting Vm and location of the cell within the cell layer and along the proximodistal axis could be factors influencing the UDS and ripple modulation. Indeed, previous studies have shown a gradient of connectivity and intrinsic cell properties along the proximodistal axis in CA3 (Q. Sun et al., 2017), and differential responses of CA1 neurons in deep and superficial layers of CA1 (Valero, Cid, et al., 2015; Valero and Prida, 2018). Analysis of the resting Vm and proximodistal location of each cell as a function of UP-DOWN modulation, as well as ripple modulation, did not reveal any significant trends, except for the fact that the most depolarized CA3 cells tend to hyperpolarize most during ripples, consistent with the fact that these cells are furthest away from the $GABA_A$ reversal potential (data not shown). However, our recordings do not span the full proximodistal axis and may hence not be ideally suited to test the dependence of our results on proximodistal location. Furthermore, we record from multiple neurons in each experiment (Figure 2.4) which does not allow us to unequivocally identify the location of each neuron within the cell layer. Future experiments can provide more conclusive evidence concerning the factors that explain the variability of subthreshold modulation by UDS and ripples across the hippocampal subfields.

These results provide novel insights into the processes of ripple initiation, build up, and termination in awake animals. Ripples occur exclusively in UP states characterized by increased entorhinal inputs to DG and associated with pronounced hyperpolarization of CA3 pyramidal cells. This suggests that broad inhibition in CA3 may be a prerequisite for ripple initiation. Furthermore, DG and CA1 pre-ripple responses suggest that ripples are not initiated as isolated events within CA3, but are the culmination of extended interplay across multiple areas. This may reflect the role of cortical inputs in influencing the neuronal patterns replayed by the hippocampus during awake ripples, consistent with their role in spatial decision making. Finally, growing hyperpolarization in CA3 throughout the course of a ripple suggests that feedback inhibition is a key feature of ripple buildup as well as termination. This may reflect a winner-take-all mechanism, by which a few neurons that fire overcoming a background of inhibition in UP states further suppress all other neurons via feedback inhibition, ensuring sparseness and selectivity of transient network pattern activation.

4.4 Methods

Ripple detection

Ripples were detected as transient increases in power in the ripple frequency band of the LFP from the probe site located in the CA1 pyramidal cell layer. Ripple power was estimated by band-pass filtering the LFP trace (80-250 Hz), smoothing its square with a Gaussian kernel (10 ms), and taking the square root. Candidate ripple events were identified as segments for which the ripple power was more than 3 s.d. above the mean. Segments that were less than 55 ms apart were merged, and after the merging step segments of length less than 20 ms were rejected as artifacts. A reference recording site away from the CA1 cell layer that does not exhibit ripples was identified and the same procedure was applied for ripple detection on this reference channel. Events detected in both the CA1 and the reference LFP trace were rejected as artifacts.

Adapting recurrent neural population model

When uncoupled, the EC and CA3 population dynamics follow the Wilson-Cowan type r-a model studied in detail in (Levenstein, Buzsáki, and Rinzel, 2019). Briefly, the mean firing rate of the EC population (rec) evolves under activity-driven adaptation (aec) according to the equations:

$$\tau_r \frac{dr}{dt} = -r + R_\infty(wr - ba + I + \xi(t)) \tag{4.1}$$

$$\tau_a \frac{dr}{dt} = -a + A_\infty(r) \tag{4.2}$$

with sigmoid activation functions $R_\infty(x)$ and $A_\infty(x)$ given by the logistic curve

$$f(x) = \frac{1}{1 + e^{-k(x-x_0)}} \tag{4.3}$$

where $k = 1,\ x_0 = 5$ for $R_\infty(x)$ and $k = 15,\ x_0 = 0.5$ for $A_\infty(x)$. The time constants $\tau_r = 1$ and $\tau_a = 25$ are dimensionless and set the arbitrary units (AU) of the time axis. For the EC population the strength of recurrent excitation (w), adaptation weight (b), and the tonic drive (I) are all constant parameters with the following values: $w = 6.8, b = 1, I = 2.1$. The model is excited by stochastic fluctuations $\xi(t)$ given by an Ornstein–Uhlenbeck process

$$d\xi_t = \theta\xi_t dt + \sigma\sqrt{2\theta}dW_t \tag{4.4}$$

with parameters $\theta = 0.05$ and $\sigma = 0.1$, corresponding to a time constant of 20 and steady-state standard deviation of σ. The mean firing rate of the CA3 population

evolves under the same equations (4.1-4.4), but the drive is now a linear function of EC activity

$$I(t) = I_0 - I_g r_{EC}(t) \tag{4.5}$$

with $I_0 = 2.5$ and $I_g = 0.6$, so that elevated EC activity generates a net inhibitory drive to CA3. The strength of recurrent excitation in CA3 is also a linear function of the EC adaptation parameter

$$w(t) = w_0 + w_g a_{EC}(t) \tag{4.6}$$

with $w_0 = 3.5$ and $w_g = 2.5$, so that the EC UP state leads to an increase in the strength of CA3 recurrent excitation. The stochastic fluctuations exciting the CA3 model have $\sigma = 0.25$ and are unrelated to those in EC.

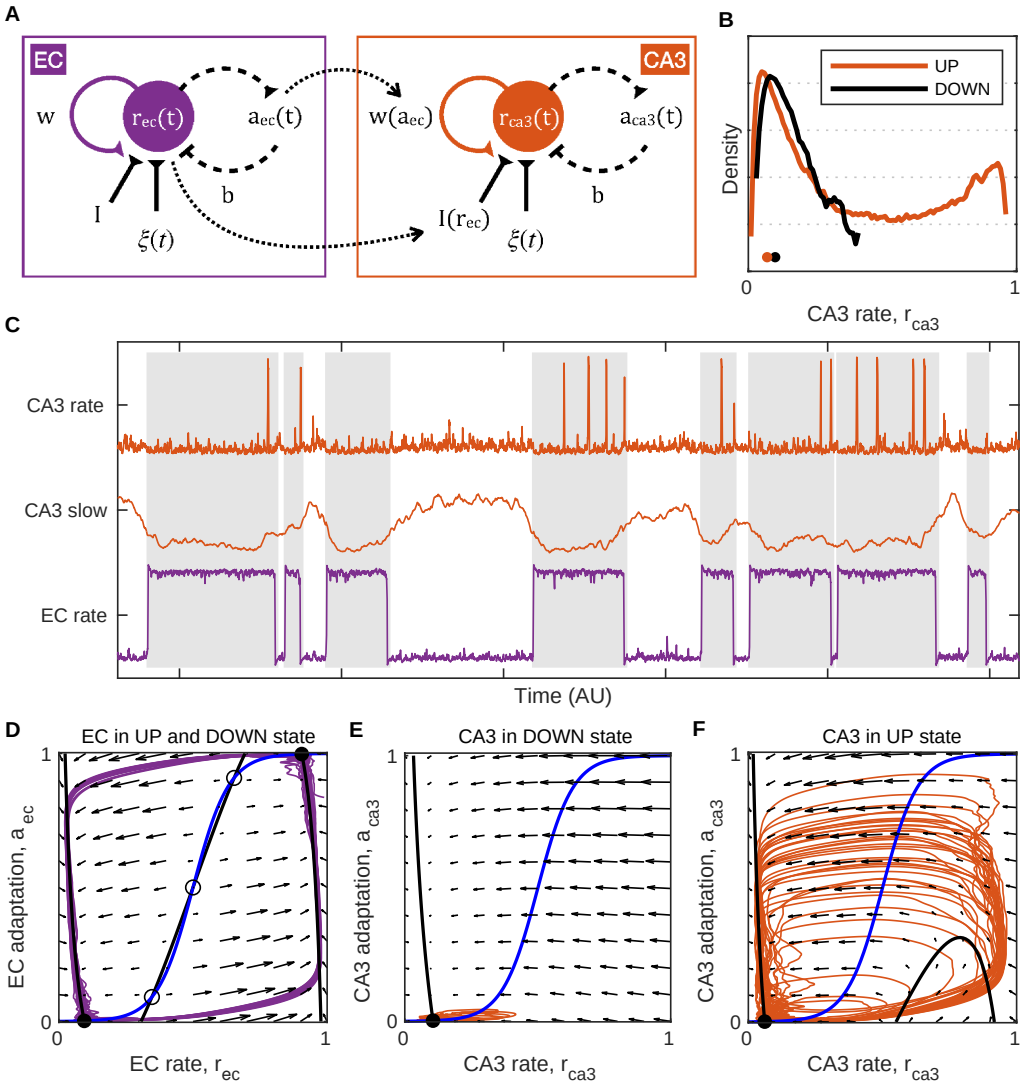

Figure 4.5: **Model of UDS Control of CA3 Network Excitability.**

Figure 4.5: **(continued)**
(A) Idealized model of EC and CA3 adapting recurrent neural populations. EC activity provides net inhibition to the CA3 population via I(rec), possibly due to feedforward inhibition or indirect influence via DG, and modulates the strength of CA3 recurrent excitation via w(aac), modeling the effects of UDS-dependent shifts in cholinergic tone on CA3 synaptic transmission.
(B) Probability density of the simulated CA3 population rate rca3 during EC UP and DOWN states. Notice that the median CA3 population rate is higher in the DOWN than the UP state (black and orange dots) despite the presence of population bursts (rate values near 1) restricted only to the UP state.
(C) Example model simulation demonstrating that the EC population exhibits UP and DOWN dynamics while the CA3 population produces transient population bursts ("ripples") restricted to the UP state (gray segments). The slow component of the CA3 rate is magnified in the middle to show that mean CA3 activity is higher during the DOWN state and lower during the UP state when population bursts occur.
(D-F) Phase plane plots of the model dynamics. The model evolution is governed by the velocity fields displayed as arrows. The model stable (filled circles) and unstable (open circles) fixed points occur at the intersections of the population rate (black) and adaptation (blue) nullclines. Model trajectories are plotted in purple and orange.
(D) EC dynamics exhibit two stable fixed points (black circles) corresponding to the UP and DOWN states with noise fluctuations driving transitions between them.
(E) CA3 dynamics in the EC DOWN state exhibit a single stable fixed point (black circle) and are not excitable, i.e. noise fluctuations cannot trigger a spike in the population rate.
(F) CA3 dynamics in the EC UP state exhibit a single stable fixed point (black circle) at a lower population rate level than in the DOWN state (E), but are excitable, i.e. noise fluctuations can trigger population spikes ("ripples").

BIBLIOGRAPHY

Acsady, Laszlo, Anita Kamondi, Attila Sık, Tamás Freund, and György Buzsáki (1998). "GABAergic cells are the major postsynaptic targets of mossy fibers in the rat hippocampus". *Journal of neuroscience* 18.9, pp. 3386–3403.

Aksay, Emre, Georgi Gamkrelidze, H Sebastian Seung, Robert Baker, and David W Tank (2001). "In vivo intracellular recording and perturbation of persistent activity in a neural integrator". *Nature neuroscience* 4.2, pp. 184–193.

Amaral, David G and Menno P Witter (1989). "The three-dimensional organization of the hippocampal formation: a review of anatomical data". *Neuroscience* 31.3, pp. 571–591.

Basu, Jayeeta, Jeffrey D Zaremba, Stephanie K Cheung, Frederick L Hitti, Boris V Zemelman, Attila Losonczy, and Steven A Siegelbaum (2016). "Gating of hippocampal activity, plasticity, and memory by entorhinal cortex long-range inhibition". *Science* 351.6269, aaa5694.

Battaglia, Francesco P, Gary R Sutherland, and Bruce L McNaughton (2004). "Hippocampal sharp wave bursts coincide with neocortical "up-state" transitions". *Learning & memory* 11.6, pp. 697–704.

Bazelot, Michaël, Maria T Teleńczuk, and Richard Miles (2016). "Single CA3 pyramidal cells trigger sharp waves in vitro by exciting interneurones". *The Journal of physiology* 594.10, pp. 2565–2577.

Buzsáki, György (1986). "Hippocampal sharp waves: their origin and significance". *Brain research* 398.2, pp. 242–252.

– (2015). "Hippocampal sharp wave-ripple: A cognitive biomarker for episodic memory and planning". *Hippocampus* 25.10, pp. 1073–1188.

Buzsáki, György, Costas A Anastassiou, and Christof Koch (2012). "The origin of extracellular fields and currents—EEG, ECoG, LFP and spikes". *Nature reviews neuroscience* 13.6, pp. 407–420.

Chen, Tianshi, Henrik Ohlsson, and Lennart Ljung (2012). "On the estimation of transfer functions, regularizations and Gaussian processes—Revisited". *Automatica* 48.8, pp. 1525–1535.

Cowan, Ronald L and Charles J Wilson (1994). "Spontaneous firing patterns and axonal projections of single corticostriatal neurons in the rat medial agranular cortex". *Journal of neurophysiology* 71.1, pp. 17–32.

Crochet, Sylvain, James FA Poulet, Yves Kremer, and Carl CH Petersen (2011). "Synaptic mechanisms underlying sparse coding of active touch". *Neuron* 69.6, pp. 1160–1175.

Davoudi, Heydar and David J Foster (2019). "Acute silencing of hippocampal CA3 reveals a dominant role in place field responses". *Nature neuroscience* 22.3, pp. 337–342.

Dayan, Peter and Laurence F Abbott (2003). "Theoretical neuroscience: computational and mathematical modeling of neural systems". *Journal of Cognitive Neuroscience* 15.1, pp. 154–155.

Edwards, Frances A, Arthur Konnerth, Bert Sakmann, and Tomoyuki Takahashi (1989). "A thin slice preparation for patch clamp recordings from neurones of the mammalian central nervous system". *Pflügers Archiv* 414.5, pp. 600–612.

Ego-Stengel, Valérie and Matthew A Wilson (2010). "Disruption of ripple-associated hippocampal activity during rest impairs spatial learning in the rat". *Hippocampus* 20.1, pp. 1–10.

Ellender, Tommas J, Wiebke Nissen, Laura L Colgin, Edward O Mann, and Ole Paulsen (2010). "Priming of hippocampal population bursts by individual perisomatic-targeting interneurons". *Journal of Neuroscience* 30.17, pp. 5979–5991.

English, Daniel F, Adrien Peyrache, Eran Stark, Lisa Roux, Daniela Vallentin, Michael A Long, and György Buzsáki (2014). "Excitation and inhibition compete to control spiking during hippocampal ripples: intracellular study in behaving mice". *Journal of Neuroscience* 34.49, pp. 16509–16517.

Evangelista, Roberta, Gaspar Cano, Claire Cooper, Dietmar Schmitz, Nikolaus Maier, and Richard Kempter (2020). "Generation of sharp wave-ripple events by disinhibition". *Journal of Neuroscience* 40.41, pp. 7811–7836.

Foster, David J (2017). "Replay comes of age". *Annual review of neuroscience* 40, pp. 581–602.

Girardeau, Gabrielle, Karim Benchenane, Sidney I Wiener, György Buzsáki, and Michaël B Zugaro (2009). "Selective suppression of hippocampal ripples impairs spatial memory". *Nature neuroscience* 12.10, pp. 1222–1223.

Hafting, Torkel, Marianne Fyhn, Sturla Molden, May-Britt Moser, and Edvard I Moser (2005). "Microstructure of a spatial map in the entorhinal cortex". *Nature* 436.7052, pp. 801–806.

Hahn, Thomas TG, James M McFarland, Sven Berberich, Bert Sakmann, and Mayank R Mehta (2012). "Spontaneous persistent activity in entorhinal cortex modulates cortico-hippocampal interaction in vivo". *Nature neuroscience* 15.11, pp. 1531–1538.

Hahn, Thomas TG, Bert Sakmann, and Mayank R Mehta (2007). "Differential responses of hippocampal subfields to cortical up–down states". *Proceedings of the National Academy of Sciences* 104.12, pp. 5169–5174.

Hamill, Owen P, A Marty, Erwin Neher, Bert Sakmann, and Frederick J Sigworth (1981). "Improved patch-clamp techniques for high-resolution current recording from cells and cell-free membrane patches". *Pflügers Archiv* 391.2, pp. 85–100.

Harvey, Christopher D, Forrest Collman, Daniel A Dombeck, and David W Tank (2009). "Intracellular dynamics of hippocampal place cells during virtual navigation". *Nature* 461.7266, pp. 941–946.

Hasselmo, Michael E and Eric Schnell (1994). "Laminar selectivity of the cholinergic suppression of synaptic transmission in rat hippocampal region CA1: computational modeling and brain slice physiology". *Journal of Neuroscience* 14.6, pp. 3898–3914.

Hasselmo, Michael E, Eric Schnell, and Edi Barkai (1995). "Dynamics of learning and recall at excitatory recurrent synapses and cholinergic modulation in rat hippocampal region CA3". *Journal of Neuroscience* 15.7, pp. 5249–5262.

Hochreiter, Sepp and Jürgen Schmidhuber (1997). "Long short-term memory". *Neural computation* 9.8, pp. 1735–1780.

Hopfield, John J (1982). "Neural networks and physical systems with emergent collective computational abilities". *Proceedings of the national academy of sciences* 79.8, pp. 2554–2558.

Horikawa, K and WE Armstrong (1988). "A versatile means of intracellular labeling: injection of biocytin and its detection with avidin conjugates". *Journal of neuroscience methods* 25.1, pp. 1–11.

Hulse, Brad K, Evgueniy V Lubenov, and Athanassios G Siapas (2017). "Brain state dependence of hippocampal subthreshold activity in awake mice". *Cell reports* 18.1, pp. 136–147.

Hulse, Brad K, Laurent C Moreaux, Evgueniy V Lubenov, and Athanassios G Siapas (2016). "Membrane potential dynamics of CA1 pyramidal neurons during hippocampal ripples in awake mice". *Neuron* 89.4, pp. 800–813.

Hunt, David L, Daniele Linaro, Bailu Si, Sandro Romani, and Nelson Spruston (2018). "A novel pyramidal cell type promotes sharp-wave synchronization in the hippocampus". *Nature neuroscience* 21.7, pp. 985–995.

Ishizuka, Norio, W Maxwell Cowan, and David G Amaral (1995). "A quantitative analysis of the dendritic organization of pyramidal cells in the rat hippocampus". *Journal of Comparative Neurology* 362.1, pp. 17–45.

Isomura, Yoshikazu, Anton Sirota, Simal Özen, Sean Montgomery, Kenji Mizuseki, Darrell A Henze, and György Buzsáki (2006). "Integration and segregation of activity in entorhinal-hippocampal subregions by neocortical slow oscillations". *Neuron* 52.5, pp. 871–882.

Jadhav, Shantanu P, Caleb Kemere, P Walter German, and Loren M Frank (2012). "Awake hippocampal sharp-wave ripples support spatial memory". *Science* 336.6087, pp. 1454–1458.

Jarosiewicz, Beata and William E Skaggs (2004). "Level of arousal during the small irregular activity state in the rat hippocampal EEG". *Journal of neurophysiology* 91.6, pp. 2649–2657.

Ji, Daoyun and Matthew A Wilson (2007). "Coordinated memory replay in the visual cortex and hippocampus during sleep". *Nature neuroscience* 10.1, pp. 100–107.

Jiang, Xi, Jorge Gonzalez-Martinez, and Eric Halgren (2019). "Coordination of human hippocampal sharpwave ripples during NREM sleep with cortical theta bursts, spindles, downstates, and upstates". *Journal of Neuroscience* 39.44, pp. 8744–8761.

Katona, Linda, Damien Lapray, Tim J Viney, Abderrahim Oulhaj, Zsolt Borhegyi, Benjamin R Micklem, Thomas Klausberger, and Peter Somogyi (2014). "Sleep and movement differentiates actions of two types of somatostatin-expressing GABAergic interneuron in rat hippocampus". *Neuron* 82.4, pp. 872–886.

Katzner, Steffen, Ian Nauhaus, Andrea Benucci, Vincent Bonin, Dario L Ringach, and Matteo Carandini (2009). "Local origin of field potentials in visual cortex". *Neuron* 61.1, pp. 35–41.

Kay, Kenneth, Marielena Sosa, Jason E Chung, Mattias P Karlsson, Margaret C Larkin, and Loren M Frank (2016). "A hippocampal network for spatial coding during immobility and sleep". *Nature* 531.7593, pp. 185–190.

Kesner, Raymond P and Edmund T Rolls (2015). "A computational theory of hippocampal function, and tests of the theory: new developments". *Neuroscience & Biobehavioral Reviews* 48, pp. 92–147.

Kim, Tony Hyun and Mark J Schnitzer (2022). "Fluorescence imaging of large-scale neural ensemble dynamics". *Cell* 185.1, pp. 9–41.

Klausberger, Thomas, Peter J Magill, László F Márton, J David B Roberts, Philip M Cobden, György Buzsáki, and Peter Somogyi (2003). "Brain-state-and cell-type-specific firing of hippocampal interneurons in vivo". *Nature* 421.6925, pp. 844–848.

Kudrimoti, Hemant S, Carol A Barnes, and Bruce L McNaughton (1999). "Reactivation of hippocampal cell assemblies: effects of behavioral state, experience, and EEG dynamics". *Journal of Neuroscience* 19.10, pp. 4090–4101.

Lee, Albert K and Matthew A Wilson (2002). "Memory of sequential experience in the hippocampus during slow wave sleep". *Neuron* 36.6, pp. 1183–1194.

Levenstein, Daniel, György Buzsáki, and John Rinzel (2019). "NREM sleep in the rodent neocortex and hippocampus reflects excitable dynamics". *Nature communications* 10.1, pp. 1–12.

Logothetis, Nikos K, O Eschenko, Y Murayama, M Augath, T Steudel, HC Evrard, M Besserve, and A Oeltermann (2012). "Hippocampal–cortical interaction during periods of subcortical silence". *Nature* 491.7425, pp. 547–553.

Lorente de Nó, Rafael (1934). "Studies on the structure of the cerebral cortex. II. Continuation of the study of the ammonic system." *Journal für Psychologie und Neurologie*.

Malezieux, Meryl, Ashley L Kees, and Christophe Mulle (2020). "Theta oscillations coincide with sustained hyperpolarization in CA3 pyramidal cells, underlying decreased firing". *Cell Reports* 32.1, p. 107868.

Margrie, Troy W, Michael Brecht, and Bert Sakmann (2002). "In vivo, low-resistance, whole-cell recordings from neurons in the anaesthetized and awake mammalian brain". *Pflügers Archiv* 444.4, pp. 491–498.

Marr, D (1971). "Simple memory: a theory for archicortex". *Philosophical Transactions of the Royal Society of London. B, Biological Sciences* 262.841, pp. 23–81.

Mathis, Alexander, Pranav Mamidanna, Kevin M Cury, Taiga Abe, Venkatesh N Murthy, Mackenzie Weygandt Mathis, and Matthias Bethge (2018). "DeepLabCut: markerless pose estimation of user-defined body parts with deep learning". *Nature neuroscience* 21.9, pp. 1281–1289.

McFarland, James M, Thomas TG Hahn, and Mayank R Mehta (2011). "Explicit-duration hidden Markov model inference of UP-DOWN states from continuous signals". *PloS one* 6.6, e21606.

Mena-Segovia, Juan, Hana M Sims, Peter J Magill, and J Paul Bolam (2008). "Cholinergic brainstem neurons modulate cortical gamma activity during slow oscillations". *The Journal of physiology* 586.12, pp. 2947–2960.

Middleton, Steven J and Thomas J McHugh (2020). "CA2: A highly connected intrahippocampal relay". *Annual Review of Neuroscience* 43, pp. 55–72.

Miles, Richard and Robert KS Wong (1983). "Single neurones can initiate synchronized population discharge in the hippocampus". *Nature* 306.5941, pp. 371–373.

Mitzdorf, Ulla (1985). "Current source-density method and application in cat cerebral cortex: investigation of evoked potentials and EEG phenomena". *Physiological reviews* 65.1, pp. 37–100.

Mizunuma, Mika, Hiroaki Norimoto, Kentaro Tao, Takahiro Egawa, Kenjiro Hanaoka, Tetsuya Sakaguchi, Hiroyuki Hioki, Takeshi Kaneko, Shun Yamaguchi, Tetsuo Nagano, et al. (2014). "Unbalanced excitability underlies offline reactivation of behaviorally activated neurons". *Nature neuroscience* 17.4, pp. 503–505.

Mölle, Matthias, Oxana Yeshenko, Lisa Marshall, Susan J Sara, and Jan Born (2006). "Hippocampal sharp wave-ripples linked to slow oscillations in rat slow-wave sleep". *Journal of neurophysiology*.

Nakazawa, Kazu, Michael C Quirk, Raymond A Chitwood, Masahiko Watanabe, Mark F Yeckel, Linus D Sun, Akira Kato, Candice A Carr, Daniel Johnston, Matthew A Wilson, et al. (2002). "Requirement for hippocampal CA3 NMDA receptors in associative memory recall". *science* 297.5579, pp. 211–218.

Neher, Erwin and Bert Sakmann (1976). "Single-channel currents recorded from membrane of denervated frog muscle fibres". *Nature* 260.5554, pp. 799–802.

Nieh, Edward H, Manuel Schottdorf, Nicolas W Freeman, Ryan J Low, Sam Lewallen, Sue Ann Koay, Lucas Pinto, Jeffrey L Gauthier, Carlos D Brody, and David W Tank (2021). "Geometry of abstract learned knowledge in the hippocampus". *Nature* 595.7865, pp. 80–84.

O'Keefe, John (1976). "Place units in the hippocampus of the freely moving rat". *Experimental neurology* 51.1, pp. 78–109.

Oliva, Azahara, Antonio Fernández-Ruiz, György Buzsáki, and Antal Berényi (2016). "Role of hippocampal CA2 region in triggering sharp-wave ripples". *Neuron* 91.6, pp. 1342–1355.

Pettersen, Klas H, Anna Devor, Istvan Ulbert, Anders M Dale, and Gaute T Einevoll (2006). "Current-source density estimation based on inversion of electrostatic forward solution: effects of finite extent of neuronal activity and conductivity discontinuities". *Journal of neuroscience methods* 154.1-2, pp. 116–133.

Pinault, Didier (1996). "A novel single-cell staining procedure performed in vivo under electrophysiological control: morpho-functional features of juxtacellularly labeled thalamic cells and other central neurons with biocytin or Neurobiotin". *Journal of neuroscience methods* 65.2, pp. 113–136.

Prida, Liset Menendez de la, Gilles Huberfeld, Ivan Cohen, and Richard Miles (2006). "Threshold behavior in the initiation of hippocampal population bursts". *Neuron* 49.1, pp. 131–142.

Roumis, Demetris K and Loren M Frank (2015). "Hippocampal sharp-wave ripples in waking and sleeping states". *Current opinion in neurobiology* 35, pp. 6–12.

Sakatani, Tomoya and Tadashi Isa (2004). "PC-based high-speed video-oculography for measuring rapid eye movements in mice". *Neuroscience research* 49.1, pp. 123–131.

Sasaki, Takuya, Verónica C Piatti, Ernie Hwaun, Siavash Ahmadi, John E Lisman, Stefan Leutgeb, and Jill K Leutgeb (2018). "Dentate network activity is necessary for spatial working memory by supporting CA3 sharp-wave ripple generation and prospective firing of CA3 neurons". *Nature neuroscience* 21.2, pp. 258–269.

Scharfman, Helen E (2007). "The CA3 "backprojection" to the dentate gyrus". *Progress in brain research* 163, pp. 627–637.

Schlingloff, Dániel, Szabolcs Káli, Tamás F Freund, Norbert Hájos, and Attila I Gulyás (2014). "Mechanisms of sharp wave initiation and ripple generation". *Journal of Neuroscience* 34.34, pp. 11385–11398.

Scoville, William Beecher and Brenda Milner (1957). "Loss of recent memory after bilateral hippocampal lesions". *Journal of neurology, neurosurgery, and psychiatry* 20.1, p. 11.

Shein-Idelson, Mark, Janie M Ondracek, Hua-Peng Liaw, Sam Reiter, and Gilles Laurent (2016). "Slow waves, sharp waves, ripples, and REM in sleeping dragons". *Science* 352.6285, pp. 590–595.

Siapas, Athanassios G, Evgueniy V Lubenov, and Matthew A Wilson (2005). "Prefrontal phase locking to hippocampal theta oscillations". *Neuron* 46.1, pp. 141–151.

Siapas, Athanassios G and Matthew A Wilson (1998). "Coordinated interactions between hippocampal ripples and cortical spindles during slow-wave sleep". *Neuron* 21.5, pp. 1123–1128.

Somogyi, Peter, Linda Katona, Thomas Klausberger, Bálint Lasztóczi, and Tim J Viney (2014). "Temporal redistribution of inhibition over neuronal subcellular domains underlies state-dependent rhythmic change of excitability in the hippocampus". *Philosophical Transactions of the Royal Society B: Biological Sciences* 369.1635, p. 20120518.

Sompolinsky, Haim, Andrea Crisanti, and Hans-Jurgen Sommers (1988). "Chaos in random neural networks". *Physical review letters* 61.3, p. 259.

Squire, Larry R (1992). "Memory and the hippocampus: a synthesis from findings with rats, monkeys, and humans." *Psychological review* 99.2, p. 195.

Stark, Eran, Lisa Roux, Ronny Eichler, Yuta Senzai, Sebastien Royer, and György Buzsáki (2014). "Pyramidal cell-interneuron interactions underlie hippocampal ripple oscillations". *Neuron* 83.2, pp. 467–480.

Steriade, Mircea, David A McCormick, and Terrence J Sejnowski (1993). "Thalamocortical oscillations in the sleeping and aroused brain". *Science* 262.5134, pp. 679–685.

Steriade, Mircea, Angel Nunez, and Florin Amzica (1993a). "A novel slow (< 1 Hz) oscillation of neocortical neurons in vivo: depolarizing and hyperpolarizing components". *Journal of neuroscience* 13.8, pp. 3252–3265.

– (1993b). "Intracellular analysis of relations between the slow (< 1 Hz) neocortical oscillation and other sleep rhythms of the electroencephalogram". *Journal of Neuroscience* 13.8, pp. 3266–3283.

Steward, Oswald, Carl Cotman, and Gary Lynch (1976). "A quantitative autoradiographic and electrophysiological study of the reinnervation of the dentate gyrus by the contralateral entorhinal cortex following ipsilateral entorhinal lesions". *Brain Research* 114.2, pp. 181–200.

Sullivan, David, Jozsef Csicsvari, Kenji Mizuseki, Sean Montgomery, Kamran Diba, and György Buzsáki (2011). "Relationships between hippocampal sharp waves, ripples, and fast gamma oscillation: influence of dentate and entorhinal cortical activity". *Journal of Neuroscience* 31.23, pp. 8605–8616.

Sun, Qian, Alaba Sotayo, Alejandro S Cazzulino, Anna M Snyder, Christine A Denny, and Steven A Siegelbaum (2017). "Proximodistal heterogeneity of hippocampal CA3 pyramidal neuron intrinsic properties, connectivity, and reactivation during memory recall". *Neuron* 95.3, pp. 656–672.

Sussillo, David and Larry F Abbott (2009). "Generating coherent patterns of activity from chaotic neural networks". *Neuron* 63.4, pp. 544–557.

Szabo, Gergely G, Xi Du, Mikko Oijala, Csaba Varga, Jack M Parent, and Ivan Soltesz (2017). "Extended interneuronal network of the dentate gyrus". *Cell reports* 20.6, pp. 1262–1268.

Tamamaki, Nobuaki and Yoshiaki Nojyo (1993). "Projection of the entorhinal layer II neurons in the rat as revealed by intracellular pressure-injection of neurobiotin". *Hippocampus* 3.4, pp. 471–480.

Tang, Wenbo and Shantanu P Jadhav (2019). "Sharp-wave ripples as a signature of hippocampal-prefrontal reactivation for memory during sleep and waking states". *Neurobiology of learning and memory* 160, pp. 11–20.

Taubin, Gabriel (1991). "Estimation of planar curves, surfaces, and nonplanar space curves defined by implicit equations with applications to edge and range image segmentation". *IEEE Transactions on Pattern Analysis & Machine Intelligence* 13.11, pp. 1115–1138.

Traub, Roger D and Richard Miles (1991). *Neuronal networks of the hippocampus*. Vol. 777. Cambridge University Press.

Tukker, John J, Bálint Lasztóczi, Linda Katona, J David B Roberts, Eleftheria K Pissadaki, Yannis Dalezios, László Márton, Limei Zhang, Thomas Klausberger, and Peter Somogyi (2013). "Distinct dendritic arborization and in vivo firing patterns of parvalbumin-expressing basket cells in the hippocampal area CA3". *Journal of neuroscience* 33.16, pp. 6809–6825.

Unal, Gunes, Michael G Crump, Tim J Viney, Tımea Éltes, Linda Katona, Thomas Klausberger, and Peter Somogyi (2018). "Spatio-temporal specialization of GABAergic septo-hippocampal neurons for rhythmic network activity". *Brain Structure and Function* 223.5, pp. 2409–2432.

Valero, Manuel, Elena Cid, Robert G Averkin, Juan Aguilar, Alberto Sanchez-Aguilera, Tim J Viney, Daniel Gomez-Dominguez, Elisa Bellistri, and Liset Menendez De La Prida (2015). "Determinants of different deep and superficial CA1 pyramidal cell dynamics during sharp-wave ripples". *Nature neuroscience* 18.9, pp. 1281–1290.

Valero, Manuel and Liset Menendez de la Prida (2018). "The hippocampus in depth: a sublayer-specific perspective of entorhinal–hippocampal function". *Current opinion in neurobiology* 52, pp. 107–114.

Vandecasteele, Marie, Viktor Varga, Antal Berényi, Edit Papp, Péter Barthó, Laurent Venance, Tamás F Freund, and György Buzsáki (2014). "Optogenetic activation of septal cholinergic neurons suppresses sharp wave ripples and enhances theta oscillations in the hippocampus". *Proceedings of the National Academy of Sciences* 111.37, pp. 13535–13540.

Vanderwolf, Case H (1969). “Hippocampal electrical activity and voluntary movement in the rat”. *Electroencephalography and clinical neurophysiology* 26.4, pp. 407–418.

Viney, Tim J, Balint Lasztoczi, Linda Katona, Michael G Crump, John J Tukker, Thomas Klausberger, and Peter Somogyi (2013). “Network state-dependent inhibition of identified hippocampal CA3 axo-axonic cells in vivo”. *Nature neuroscience* 16.12, pp. 1802–1811.

Vogt, Kaspar E and Wade G Regehr (2001). “Cholinergic modulation of excitatory synaptic transmission in the CA3 area of the hippocampus”. *Journal of Neuroscience* 21.1, pp. 75–83.

Werbos, Paul J (1990). “Backpropagation through time: what it does and how to do it”. *Proceedings of the IEEE* 78.10, pp. 1550–1560.

Wierzynski, Casimir M, Evgueniy V Lubenov, Ming Gu, and Athanassios G Siapas (2009). “State-dependent spike-timing relationships between hippocampal and prefrontal circuits during sleep”. *Neuron* 61.4, pp. 587–596.

Wilson, Matthew A and Bruce L McNaughton (1994). “Reactivation of hippocampal ensemble memories during sleep”. *Science* 265.5172, pp. 676–679.

Yamamoto, Jun and Susumu Tonegawa (2017). “Direct medial entorhinal cortex input to hippocampal CA1 is crucial for extended quiet awake replay”. *Neuron* 96.1, pp. 217–227.

Ylinen, Aarne, Anatol Bragin, Zoltán Nádasdy, Gábor Jandó, I Szabo, A Sik, and György Buzsáki (1995). “Sharp wave-associated high-frequency oscillation (200 Hz) in the intact hippocampus: network and intracellular mechanisms”. *Journal of Neuroscience* 15.1, pp. 30–46.

Ziv, Yaniv, Laurie D Burns, Eric D Cocker, Elizabeth O Hamel, Kunal K Ghosh, Lacey J Kitch, Abbas El Gamal, and Mark J Schnitzer (2013). “Long-term dynamics of CA1 hippocampal place codes”. *Nature neuroscience* 16.3, pp. 264–266.

Zucca, Stefano, Marilena Griguoli, Meryl Malézieux, Noëlle Grosjean, Mario Carta, and Christophe Mulle (2017). “Control of spike transfer at hippocampal mossy fiber synapses in vivo by GABAA and GABAB receptor-mediated inhibition”. *Journal of Neuroscience* 37.3, pp. 587–598.